

This is the accepted manuscript made available via CHORUS. The article has been published as:

# Aberration-free imaging of inelastic-scattering spectra with x-ray echo spectrometers

Manuel Sánchez del Río and Yuri Shvyd'ko

Phys. Rev. A **99**, 053839 — Published 24 May 2019

DOI: [10.1103/PhysRevA.99.053839](https://doi.org/10.1103/PhysRevA.99.053839)

# Aberration-free imaging of inelastic scattering spectra with x-ray echo spectrometers

Manuel Sánchez del Río<sup>1,\*</sup> and Yuri Shvyd'ko<sup>2,†</sup>

<sup>1</sup>*ESRF, The European Synchrotron, Grenoble, France*

<sup>2</sup>*Advanced Photon Source, Argonne National Laboratory, Argonne, Illinois, USA*

(Dated: April 18, 2019)

We study conditions for aberration-free imaging of inelastic x-ray scattering (IXS) spectra with x-ray echo spectrometers. Aberration-free imaging is essential for achieving instrumental functions with high resolution and high contrast. Computational ray tracing is applied to a thorough analysis of a 0.1-meV/0.07-nm<sup>-1</sup>-resolution echo-type IXS spectrometer operating with 9-keV x-rays. We show that IXS spectra imaged by the x-ray echo spectrometer that uses lenses for the collimating and focusing optics are free of aberrations. When grazing-incidence mirrors (paraboloidal, parabolic Kirkpatrick-Baez, or parabolic Montel) are used instead of the lenses, the imaging system reveals some defocus aberration that depends on the inelastic energy transfer. However, the aberration-free images can be still recorded in a plane that is tilted with respect to the optical axis. This distortion can be thus fully compensated by inclining appropriately the x-ray imaging detector, which simultaneously improves its spatial resolution. A full simulation of imaging IXS spectra from a realistic sample demonstrates the excellent performance of the proposed designs.

PACS numbers: 41.50.+h, 07.85.Nc, 78.70.Ck

## I. INTRODUCTION

X-ray echo spectroscopy [1], a space-domain counterpart of neutron spin echo [2], was introduced recently to overcome the limitations in spectral resolution and weak signals of the traditional inelastic hard x-ray scattering (IXS) probes. X-ray echo spectroscopy is an extension into the hard x-ray domain of the approach proposed [3] and demonstrated in the soft x-ray domain [4]. X-ray echo is refocusing the defocused x-ray source image. Defocusing and refocusing systems are the main components of x-ray echo spectrometers. They are composed of focusing and dispersing optical elements, where the latter are asymmetrically cut crystals in Bragg diffraction. The optical elements have to be complemented by the x-ray source, sample, and x-ray position-sensitive detector, as schematically shown in Fig. 1. Refocusing takes place only when the defocusing and the refocusing systems compose a time-reversed pair. This implies that a virtual source placed into the detector plane produces the defocused image in the sample plane with the same linear dispersion rate as the real source.

When the defocused x-rays are scattered inelastically from the sample with an energy transfer  $\varepsilon$ , they pass through the refocusing system that refocuses them on the detector, but with a lateral shift with respect to the optical axis that is proportional to  $\varepsilon$ , see Fig. 1( $\mathbf{v}_i$ ). This property enables echo spectrometers to image IXS spectra with a spectral resolution solely determined by the sharpness of the refocused image of the source, and completely independent of the spectral composition of x-rays incident on the sample. The spectral resolution

of x-ray echo spectrometers is therefore decoupled from the spectrometer bandwidth, x-ray monochromatization is not required, and the IXS refocusing (imaging) system is broadband. These features of echo spectrometers are in a striking contrast to present-day narrow-band scanning IXS spectrometers (see [5] for a review), whose spectral resolution is determined by the smallness of the monochromator and analyzer bandwidths. As a result, broadband imaging echo-type IXS spectrometers have the potential of increasing the signal strength by orders of magnitude, thus reducing acquisition times and substantially improving spectral resolution.

The ability of the refocusing system to produce sharp and undeformed images for each inelastic  $\varepsilon$ -component is critical for achieving the high-resolution and high-contrast instrumental functions of echo-type spectrometers. This is, however, a challenge, because the defocused source image on the sample and the refocused IXS image on the detector are spread laterally with respect to the optical axis. Therefore, x-ray echo spectrometers must be truly aberration-free imaging systems capable of producing sharp images when the focusing elements are illuminated both on-axis or off-axis.

The theory of x-ray echo spectrometers developed in [1, 6] is based on paraxial analytical ray tracing, which uses ray transfer matrix analysis. It predicts aberration-free imaging, provided ideal (perfectly focusing and non-absorbing) parabolic x-ray lenses are used, which make sure that the collimating and focusing elements form a truly imaging optical system. This conclusion is also supported by computational wave propagation studies [7] performed with SRW code [8] for a 0.1-meV-resolution x-ray echo spectrometer with the parameters from [1].

Real parabolic x-ray compound refractive lenses (CRL) [9] have small effective geometrical aperture for the x-ray echo spectrometers because of photo absorption. Curved grazing incidence mirrors may feature much larger aper-

---

\*Electronic address: [srio@esrf.eu](mailto:srio@esrf.eu)

†Electronic address: [shvydko@anl.gov](mailto:shvydko@anl.gov)

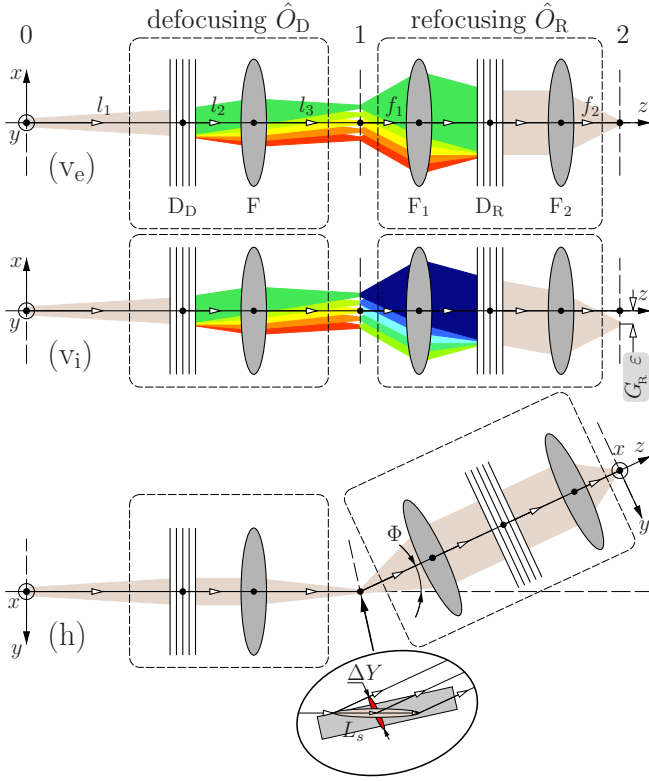


FIG. 1: Optical scheme of an x-ray echo spectrometer, composed of the defocusing  $\hat{O}_D$  and refocusing  $\hat{O}_R$  dispersing-focusing systems; the x-ray source in reference plane 0; the sample in 1; and the pixel detector in 2. The spectrometer is shown in the vertical  $(x, z)$  dispersion plane for elastic ( $v_e$ ) and inelastic ( $v_i$ ) scattering cases, as well as in the horizontal  $(y, z)$  nondispersive scattering plane (h) with the refocusing system at a scattering angle  $\Phi$  defining the momentum transfer  $Q = 2K \sin(\Phi/2)$  in scattering of a photon with an angular wavenumber  $K$ . See text for more details.

tures. However, mirrors are not good imaging devices. The Abbe sine condition, which defines the constraints that any perfect imaging system must comply with, states in particular the impossibility of building an imaging system with a single mirror. At least two reflectors are needed. In the x-ray regime, the use of Wolter-type grazing incidence mirror-pairs [10, 11] may ensure perfect imaging. The Abbe sine condition in connection with the refocusing system of x-ray echo spectrometers made up of a pair of paraboloidal mirrors with the dispersing system in between was discussed in [6] limited, however, to 1D mirrors.

The present studies aim at identifying conditions for aberration-free IXS imaging by echo-type IXS spectrometers with real 2D-mirror and lens systems. It uses geometrical 3D ray tracing of systems composed of crystals, mirrors, or lenses, including calculation of crystal reflectivity and lens absorption. The calculations are performed using the x-ray optics modeling package SHADOW [12] and its graphical user interface ShadOUI [13] available in the software suite for x-ray optics

and synchrotron beamline simulations OASYS [14].

The paper is organized as follows. In Sec. II we present the basic principles of x-ray echo spectrometers, as well as the optical design and parameters of the studied spectrometer with a 0.1-meV spectral and an  $0.07 \text{ nm}^{-1}$  momentum-transfer resolution. In Sec. III we present results of studies of IXS imaging with lenses, using both ideal focusing lenses and a full simulation of an array of real paraboloidal compound refractive lenses. Sec. IV is devoted to studies of IXS imaging using grazing incidence mirror systems, starting first with a case of imaging elastic signals in Sec. IV A, and then imaging inelastic signals in Sec. IV B, where image aberrations produced in the image plane – Sec. IV B 1 – are corrected if recorded by a detector in an oblique plane – Sec. IV B 2. Effects of glancing angle of incidence and mirrors' slope errors on the spectral resolution are discussed in Sec. IV C and Sec. IV D, respectively. Full simulations of imaging IXS spectra from realistic samples are performed in Sec. V to verify the performance of the proposed design.

## II. PRINCIPLES, OPTICAL DESIGN, AND PARAMETERS OF X-RAY ECHO SPECTROMETERS

Here, we review the principles of x-ray echo spectrometers, and the optical scheme defining in detail the configuration and elements used in the numerical simulations.

### A. Basic principles and optical scheme

The optical scheme of the x-ray echo spectrometer considered here is shown in Fig. 1. Its performance was discussed in detail and substantiated by analytical ray tracing in [1, 6].

As a result of propagation through the defocusing system  $\hat{O}_D$ , x-rays from the source with a vertical size  $\Delta x_0$  in reference plane 0 are focused on the sample in reference plane 1 with an image size  $\Delta x_1 = A_D \Delta x_0$  ( $A_D$  is a magnification factor), albeit, with the focal spot location dispersed in vertical direction  $x$  for different spectral components with a linear dispersion rate  $G_D$ .

All spectral components of the defocused source image can be refocused into a single spot (echo) with a size  $\Delta x_2 = A_R \Delta x_1$  in the detector reference plane 2 by propagation through the refocusing system  $\hat{O}_R$ , provided it is a time-reversed counterpart of the defocusing system  $\hat{O}_D$ . The latter means that x-rays from a virtual source of size  $\Delta x_2$  in the detector plane being propagated in the reverse direction produce on the sample exactly the same defocused image as the image by the defocusing system. This is expressed by the refocusing condition

$$G_D + G_R/A_R = 0, \quad (1)$$

where,  $G_R$  is a linear dispersion rate and  $A_R$  a magnification factor of the refocusing system.

Defocusing system										Refocusing system						
$G_D$	$l$	$l_1$	$l_2$	$l_3$	$A_D$	$\mathcal{D}_{\cup_D}$	$b_{\cup_D}$	$f$		$G_R$	$A_R$	$f_1$	$\frac{\mathcal{D}_{\cup_R}}{b_{\cup_R}}$	$b_{\cup_R}$	$f_2$	$A_D A_R$
$\frac{\mu\text{m}}{\text{meV}}$	m	m	m	m		$\frac{\mu\text{rad}}{\text{meV}}$		m		$\frac{\mu\text{m}}{\text{meV}}$		m	$\frac{\mu\text{rad}}{\text{meV}}$		m	
$\mp 50$	35	32.55	0.73	1.72	-0.095	-31.7	1.96	1.45		$\mp 50$	-1.0	0.4	-125	0.27	1.471	0.095

TABLE I: Global optical parameters of an x-ray echo spectrometer with a 0.1-meV spectral and a  $0.07 \text{ nm}^{-1}$  momentum-transfer resolution, see Fig. 1 for the optical scheme and the text for notations. The following parameters are fixed: monochromatic source size on the sample  $\Delta x_1 = 5 \mu\text{m}$ , the source to sample distance  $l = l_1 + l_2 + l_3$ , and the focal lengths  $f$ ,  $f_1$ . Other parameters are chosen to ensure the 0.1-meV design spectral resolution, Eqs. (2) and (6), to fulfill the refocusing condition, Eq. (1) and Eqs. (3)-(4). The central photon energy of the incident x-rays on the sample is  $E_0 = 9137.01 \text{ eV}$ , defined by (008) Bragg reflections from the Si crystals in the dispersing elements (see Figs. 11-12, and Table VI of Appendix A).

If inelastic scattering takes place on the sample with an energy transfer  $\varepsilon$ , the dispersed signal is still refocused into a tight echo signal, but laterally shifted by  $\delta x_2 = G_R \varepsilon$  in the detector plane, as shown schematically in Fig. 1(v<sub>i</sub>). This effect enables imaging IXS spectra with an energy resolution

$$\Delta\varepsilon = \Delta x_2 / |G_R| \equiv \Delta x_1 / |G_D|, \quad (2)$$

where  $\Delta\varepsilon$  corresponds to an energy transfer resulting in a lateral shift  $\delta x_2$  that is equal to the image size  $\Delta x_2$ . One of the major purposes of the paper is to verify by detailed numerical simulations the capability of x-ray echo spectrometers to image IXS spectra with the spectral resolution given by Eq. (2).

The main components of the defocusing and refocusing systems are the dispersing elements  $D_D$  and  $D_R$  and focusing elements  $F$ ,  $F_1$ , and  $F_2$ . The dispersing elements are characterized by the cumulative angular dispersion rates  $\mathcal{D}_{\cup_D}$  and  $\mathcal{D}_{\cup_R}$ , cumulative asymmetry parameters  $b_{\cup_D}$  and  $b_{\cup_R}$ , and spectral bandwidths  $\Delta E_D$  and  $\Delta E_R$ , respectively, see [1, 6] for details. The focusing elements are characterized by the focal lengths  $f$ ,  $f_1$ , and  $f_2$ . These parameters determine [1, 6] the linear dispersion rate  $G_D$  and the magnification factor  $A_D$  of the defocusing system

$$A_D = -\frac{\sigma_D l_3}{b_{\cup_D} l_{12}}, \quad G_D = \sigma_D \mathcal{D}_{\cup_D} \frac{l_3 l_1}{b_{\cup_D}^2 l_{12}}, \quad (3)$$

$$\frac{1}{f} = \frac{1}{l_{12}} + \frac{1}{l_3}, \quad l_{12} = \frac{l_1}{b_{\cup_D}^2} + l_2, \quad (4)$$

and of the refocusing system

$$G_R = \sigma_R \mathcal{D}_{\cup_R} f_2, \quad A_R = -\frac{b_{\cup_R} f_2}{f_1}. \quad (5)$$

Compared to [1, 6], we use here additional parameters  $\sigma_X = +1$  if lenses are used as focusing elements, or alternatively  $\sigma_X = -1$  for mirrors. Here  $X=D$  or  $X=R$ .

Using Eq. (5), the spectral resolution  $\Delta\varepsilon$  given by Eq. (2) can be equivalently expressed through the pa-

rameters of the refocusing system as

$$\Delta\varepsilon = \frac{|b_{\cup_R}|}{|\mathcal{D}_{\cup_R}|} \frac{\Delta x_1}{f_1}. \quad (6)$$

In the present paper we are studying a particular case of an x-ray echo spectrometer with a 0.1-meV spectral and a  $0.07 \text{ nm}^{-1}$  momentum-transfer resolution employing 9.1-keV x-rays with design parameters provided in [6]. The global optical parameters of the x-ray echo spectrometer are summarized in Table I and discussed in the following sections.

## B. From source to sample: defocusing system

The vertical source size is typically  $\Delta x_0 \simeq 25 \mu\text{m}$  [full width at half maximum (FWHM)] for state of the art undulator synchrotron radiation sources. Assuming a focusing system with a magnification factor  $|A_D| \simeq 0.1$ , we expect for the monochromatic beam size on the sample  $\Delta x_1 = |A_D| \Delta x_0 \simeq 2.5 \mu\text{m}$ . Because the high-heat-load monochromator (installed upstream of the defocusing system, not shown in Fig. 1) may degrade the wavefront, we use in our simulations a more conservative value  $\Delta x_1 = 5 \mu\text{m}$ . This value together with the design spectral resolution  $\Delta\varepsilon = 0.1 \text{ meV}$  of the x-ray echo spectrometer determine via Eq. (2) the required value of the linear dispersion rate  $|G_D| = 50 \mu\text{m/meV}$ .

Focusing element  $F$  should possess properties of the true imaging system. We assume it to be a paraboloidal compound refractive lens (CRL), in a good approximation the truly imaging optic [9]. Its focal length  $f = 1.446 \text{ m}$  can be realized using 17 double-convex 2D Beryllium lenses of  $200 \mu\text{m}$  radius of curvature. This chosen configuration gives an effective geometrical aperture of  $660 \mu\text{m}$ , comparable to the size of the intercepted undulator beam.

In our studies, we fix the value of  $f$  as well as the source-to-sample distance  $l = l_1 + l_2 + l_3 = 35 \text{ m}$ . The values of other parameters of the defocusing system, see Table I, such as  $\mathcal{D}_{\cup_D}$ ,  $b_{\cup_D}$ ,  $l_1$ ,  $l_2$ ,  $l_3$ , and  $A_D$  are not

unique, but are chosen to be practical and to meet the constraints imposed by Eqs. (1)-(4).

The dispersing element  $D_D$  has to be chosen to meet the values of  $\mathcal{D}_{U_D}$  and  $b_{U_D}$  provided in Table I. The required big angular dispersion rate  $\mathcal{D}_{U_D} = -31.7 \mu\text{rad}/\text{meV}$  can be achieved only by using multi-crystal systems featuring the enhancement effect of angular dispersion [15, 16].<sup>1</sup> Considered in the present studies four-crystal dispersing element was discussed in detail in [6]. Its optical scheme and spectral transmission function are also shown in Fig. 11 of Appendix A.

### C. From sample to detector: refocusing system

The refocusing system is composed of a pair of focusing elements  $F_1$ ,  $F_2$ , and a dispersing element  $D_R$  placed in between, see Fig. 1.

The focal length of  $F_1$  is chosen to be  $f_1 = 0.4$  m, defined by the desired momentum transfer resolution of  $\Delta Q = 0.07 \text{ nm}^{-1}$ , see below. According to Eq. (6), this value of  $f_1$  together with the design spectral resolution  $\Delta\varepsilon = 0.1$  meV and the fixed value of the secondary monochromatic source size  $\Delta x_1 = 5 \mu\text{m}$  requires that  $\mathcal{D}_{U_R}/b_{U_R} = -125 \mu\text{rad}/\text{meV}$ . The negative sign results from Eqs. (1) and (5). A four-crystal dispersing element with the required value of  $\mathcal{D}_{U_R}/b_{U_R}$  was discussed in detail in [6]. Its optical scheme and spectral transmission function are also shown in Fig. 12 of Appendix A.

The refocusing system is designed to provide 1:1 imaging (magnification factor  $A_R = -1$ ) of the secondary source in the intermediate image plane 1 to image plane 2. This is favored by the Abbe sine condition, see discussion in [6] for details. This condition along with the previously defined values of  $f_1$  and  $b_{U_R}$  require  $f_2 = 1.471$  m, see Eq. (5). In fact, the significance of the 1:1 magnification for aberration-free imaging of the IXS spectra is one of the central questions to be addressed by numerical simulations. Deviations from 1:1 imaging will be studied as well. The specific case of  $A_R = -1$  requires  $G_R = G_D = -50 \mu\text{m}/\text{meV}$  and  $\Delta x_2 = |A_D|\Delta x_0 \equiv \Delta x_1 = 5 \mu\text{m}$ .

We study IXS imaging with different types of focusing elements  $F_1$  and  $F_2$ : ideal lenses, 2D paraboloidal compound refractive lenses [9], 2D paraboloidal mirrors [20], or compound 2D mirror systems composed of 1D parabolic mirrors, such as Kirkpatrick-Baez (KB) [21] or

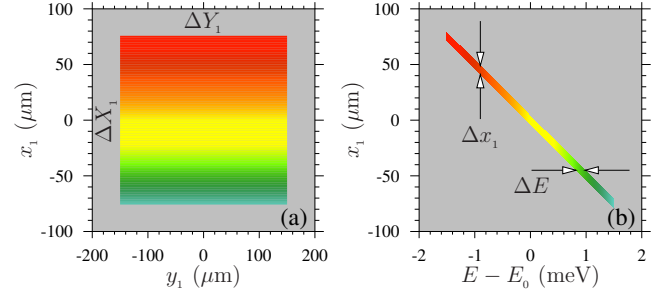


FIG. 2: (a) Virtual secondary source in reference sample plane 1 featuring photon energy dispersion in the vertical ( $x$ ) direction with a linear dispersion rate  $G_D = -50 \mu\text{m}/\text{meV}$ . Source dimensions are  $\Delta X = 150 \mu\text{m}$  and  $\Delta Y = 300 \mu\text{m}$ . (b) Each horizontal line is a source of photons with a Gaussian spectral spread of  $\Delta E = 0.1$  meV (FWHM). Each monochromatic component has a vertical Gaussian spread (monochromatic source size) of  $\Delta x_1 = 5 \mu\text{m}$  (FWHM).

Montel [22]. The mirrors are considered to be coated with laterally graded multilayers similar to those used in [23, 24], providing a large glancing angle of incidence  $\varphi \simeq 20 - 30$  mrad. Due to the large  $\varphi$ , the mirrors are compact, have a large geometrical aperture, and most importantly mitigate aberrations, as discussed in [6]. Impacts of the magnitude of  $\varphi$  and of the mirrors' slope errors on the IXS imaging will be studied.

### D. Description of the sample, a secondary source for the refocusing system

X-rays scattered from the sample are seen by the refocusing system as emanating from a secondary three-dimensional source. Studies [1, 6, 7] show that the performance of the refocusing system is relatively insensitive to the secondary source position along the optical axis. In particular, the tolerance on the position variation is at least a few millimeters in the present case of the 0.1-meV spectrometer. Therefore, if the sample thickness is much smaller, the secondary source can be considered with high accuracy to be flat and distributed only in plane  $(x, y)$ . Such an approximation is used here.

The defocusing system focuses each spectral component  $E$  to a spot of a vertical size  $\Delta x_1$ , see Figs. 1( $v_e$ )-1( $v_i$ ), with the locations linearly dispersed as

$$x_1(E) = G_D(E - E_0). \quad (7)$$

In the elastic scattering process, the photon energy of the secondary source is the same as that of the incident one, as indicated in Fig. 1( $v_e$ ). To simulate inelastic scattering with an energy transfer  $\varepsilon$ , we modify the energy of the x-ray scattered by the sample as

$$E_0 \rightarrow E_0 + \varepsilon. \quad (8)$$

This presentation may mean that inelastic x-ray scattering with an energy transfer  $\varepsilon$  takes place in all scattering

<sup>1</sup> Diffraction gratings are not practical dispersing elements in the hard x-ray regime. Instead, crystals in Bragg diffraction can function as gratings, dispersing x-rays into spectral fans with photons of different energies propagating at different angles [17–19]. The grating effect takes place only in asymmetric Bragg diffraction, with the diffracting atomic planes at a nonzero angle  $\eta \neq 0$  to the entrance crystal surface. Bragg diffraction ensures high reflectivity, while the asymmetric cut results in electron density periodic modulation along the crystal surface responsible for the grating effect of angular dispersion.



points simultaneously, as indicated in Fig. 1(v<sub>i</sub>). This is not actually the case. However, this presentation is still valid if a time-averaged picture is assumed.

Because the angular acceptance of the refocusing system is limited to  $\Delta\theta_R \simeq 260 \mu\text{rad}$  [6], it can “see” only  $\Delta\theta_R f_1 \simeq 100 \mu\text{m}$  of the secondary source. We restrict therefore the total vertical size of the secondary source in our simulations to  $\Delta X_1 = 150 \mu\text{m}$ , see Fig. 2(a). This corresponds to a maximal spectral variation of  $E - E_0 = \pm 1.5 \text{ meV}$  in the incident beam, see Fig. 2(b).

If the scattering angle  $\Phi$  is small, see Fig. 1(h), the horizontal secondary source size is equal to the horizontal focal spot size on the sample, which can be just a few micrometers. However, with a finite penetration length  $L_s$ , the horizontal secondary source size  $\Delta Y_1 = L_s \sin \Phi$  grows with  $\Phi$ , as shown in the inset of Fig. 1(h). For practical reasons, which cover many cases, we assume in our simulations  $\Delta Y_1 = 300 \mu\text{m}$ .

Each point on the sample is a secondary source emitting isotropically (a spherical wave). But only a small part of the radiation will be accepted by the refocusing system (defined by the angular aperture of the system and possible use of secondary slits to control the momentum resolution). Here we limit the angular spread of the photons from the sample to 1.5 mrad in both the vertical  $\Upsilon_v$  and horizontal  $\Upsilon_h$  planes. This is consistent with the desired momentum transfer resolution  $\Delta Q = \Upsilon Q = 0.07 \text{ nm}^{-1}$  for the 0.1-meV spectrometer, where  $\Upsilon = \max[\Upsilon_v, \Upsilon_h]$ .

### III. IXS IMAGING WITH LENSES

In the first step, we study how the extended two-dimensional x-ray source dispersed in the vertical direction in reference plane 1, see Figs. 1 and 2, is imaged in reference plane 2 by the refocusing system composed of non-absorbing perfect paraboloidal lenses used as the collimating  $F_1$  and focusing  $F_2$  optical elements and of the CDDW dispersing element in between.

According to Fig. 1, we expect the refocusing system to focus all vertically dispersed monochromatic components into one spot, with the linear dispersion annihilated. In the perfect case, the vertical distribution should be Gaussian with a width  $\Delta x_2$  equal to the monochromatic source size  $\Delta x_1 = 5 \mu\text{m}$ , assuming the designed 1:1 imaging in the vertical plane, which takes into account the combined effect of lenses and crystals ( $A_R = -b_{UR} f_2/f_1 = -1$ ). The source image size in the horizontal direction is defined by the focal lengths of the lenses only: the magnification factor is  $f_2/f_1 = 3.678$ , thus the image size in the horizontal plane is  $\Delta Y_2 = \Delta Y_1 (f_2/f_1) = 1103 \mu\text{m}$ . This picture turns out, however, to be incomplete.

Figure 3(a) shows the cross section of the beam calculated in image plane 2 in the case of elastic scattering ( $\varepsilon = 0$ ), related to Fig. 1(v<sub>e</sub>). Its horizontal width  $\Delta \tilde{Y}_2$  agrees with  $\Delta Y_2$  (we are using tilde throughout the paper to indicate values calculated numerically). The vertical

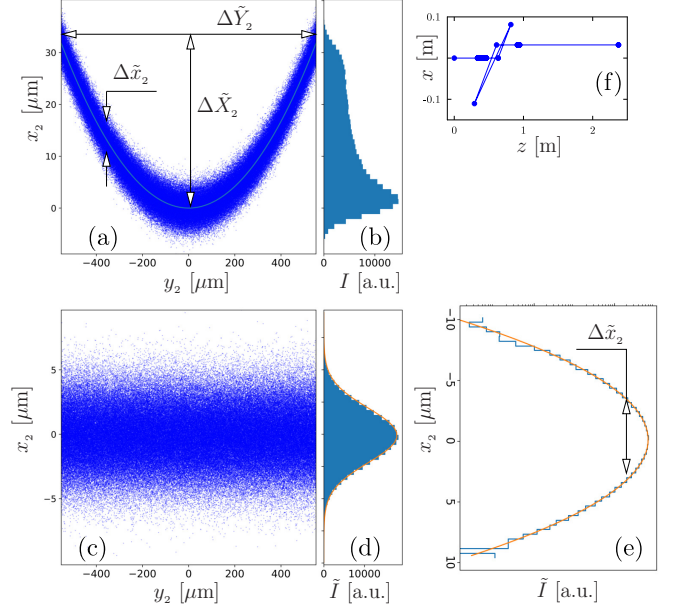


FIG. 3: (a) Cross section of the beam in image plane 2 rendered by the refocusing system composed of two ideal lenses and the CDDW dispersing element in between. The solid line represents a parabolic fit to the beam profile. (b) Vertical profile  $I(x_2)$  obtained from (a) by integration over the horizontal coordinate  $y_2$ . (c) Beam cross section of (a) with the parabolic fit removed. (d) Vertical profile  $\tilde{I}(x_2)$  obtained from (c) with a Gaussian fit (brown line). (e) Vertical profile  $\tilde{I}(x_2)$  (c) shown on the logarithmic scale. (f) Side view of the beam trajectory (optical axis). Angular apertures  $\Upsilon_h = \Upsilon_v = 1.5 \text{ mrad}$ .

profile at any  $y_2$  has a distribution which fits perfectly to the Gaussian function with a width  $\Delta \tilde{x}_2 \simeq 4.95 \mu\text{m}$  (FWHM), which is very close to that expected from the paraxial theory image vertical size  $\Delta x_2 = 5 \mu\text{m}$ . However, the whole image is curved to a parabolic shape. This happens due to Bragg reflections from the crystals in the dispersing element  $D_R$ , see [6, 7] for details.

A 1D (strip) detector would measure a distribution shown in Fig. 3(b) with a vertical spread  $\Delta \tilde{X} \simeq 32 \mu\text{m}$  much larger than  $\Delta x_2 = 5 \mu\text{m}$ , and therefore would result in an asymmetric and much broadened instrumental spectral function. The detrimental effect of the curvature is significant only if the horizontal secondary source size is large, as in the case considered here of  $\Delta Y_1 = 300 \mu\text{m}$ .

The problem can be circumvented by using a 2D pixel detector and the following data evaluation [6]. The image in Fig. 3(a) is flattened by subtracting the best fit parabola  $x_2 = \Pi y_2^2 + x_2(0)$  and integrating over  $y_2$ . The resulting reduced vertical profile, shown in Fig. 3(c), fits to a Gaussian function over an intensity range of at least four orders of magnitude with a width  $\Delta \tilde{x}_2 = 4.95 \pm 0.02 \mu\text{m}$  (FWHM), which is in a very good agreement with the expected  $\Delta x_2 = 5 \mu\text{m}$ .

Further simulations show that this picture remains valid also in the case of inelastic x-ray scattering with nonzero energy transfer  $\varepsilon \neq 0$ . What changes is the

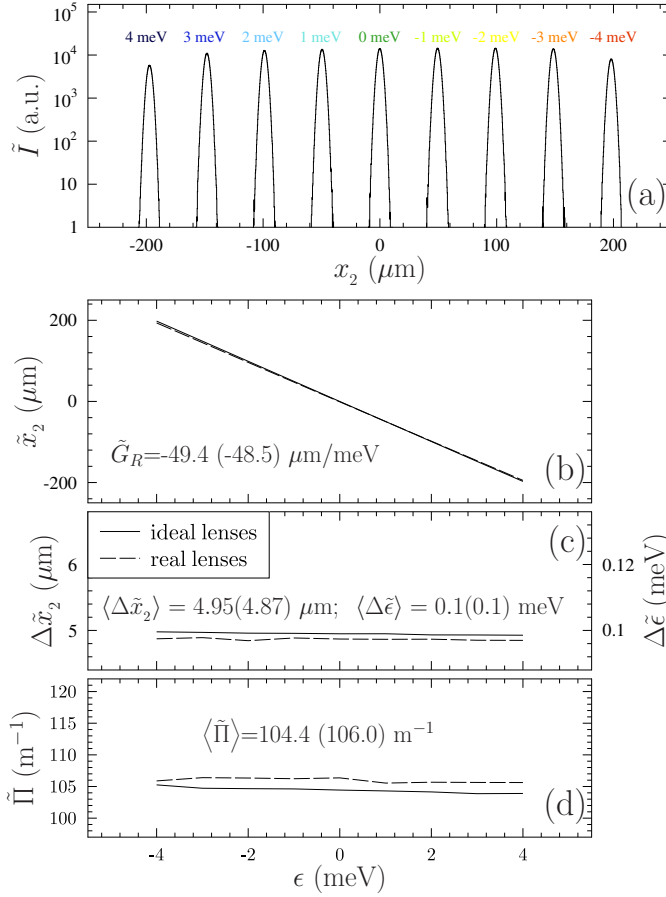


FIG. 4: Performance characteristics of the x-ray echo spectrometer with the refocusing system composed of ideal lenses or real CRLs as focusing elements: (a) Reduced image profiles calculated for various values of energy transfer  $\varepsilon$  in inelastic x-ray scattering under the same conditions as in Fig. 3. (b) Image peak position  $\tilde{x}_2$ , (c) reduced image size  $\Delta\tilde{x}_2$  and (d) curvature  $\tilde{\Pi}$  of the best-fit parabola to the image profile as a function of  $\varepsilon$ . Solid lines present results for the ideal lenses, while dashed lines and values in parentheses are for the real CRLs.

position of the image, which shifts linearly with  $\varepsilon$  in the vertical direction along  $x_2$  with a linear dispersion rate  $\tilde{G}_R = -49.4 \mu\text{m}/\text{meV}$ , see Figs. 4(a)-(b), in agreement with that predicted by the paraxial theory  $G_R = -50 \mu\text{m}/\text{meV}$ . The reduced image size and therefore the spectral resolution of the spectrometer is independent of  $\varepsilon$ , see Fig. 4(c). The results of Figs. 4(a)-(c) confirm one of the key properties of x-ray echo spectrometers: their capability of imaging IXS spectra with high resolution and contrast.

Figure 4(d) demonstrates another important feature: the curvature  $\tilde{\Pi}$  of the best-fit parabola to the image profile is practically independent of  $\varepsilon$ . This is in agreement with the theory [6], which predicts that  $\Pi = UA_R/2f_2^2$ , where  $U = f_1(1 - b_2b_3)/|b_1b_2b_3|\cos\theta_2$ , and therefore that  $\Pi$  is an invariant of the refocusing system, independent

of the IXS energy transfer  $\varepsilon$ . Due to this, the curvature  $\Pi$  can be determined in practice from the elastic signal and applied to flatten numerically the inelastic signals, and thus to overcome degradation of the spectral function and resolution due to the large horizontal size of the secondary source. With the parameters of the spectrometer considered here we calculate  $\Pi = 102 \text{ m}^{-1}$  and  $\Delta X_2 = \Pi(\Delta Y f_2/2f_1)^2 = 31 \mu\text{m}$ , which are close to  $\tilde{\Pi} = 104.4 \text{ m}^{-1}$  and  $\Delta\tilde{X} = 32 \mu\text{m}$  calculated numerically for the ideal lenses, see Figs. 3(a) and 4(c).

The picture does not change if realistic absorbing parabolic compound refractive lenses are used [9] instead of the ideal lens. The appropriate results of simulations are shown by dashed lines in Figs. 4(b)-(d). The only major difference is in the signal strength, which is reduced by a factor of 41 (assuming  $\Upsilon_v \times \Upsilon_h = 1.5 \times 1.5 \text{ mrad}^2$  angular divergence of x-rays from the source) because of the effective geometrical aperture reduced by photo-absorption.

Here we conclude that the refocusing system composed of parabolic lenses represents an aberration-free imaging system capable of making sharp images of IXS spectra.

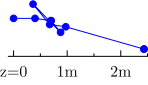
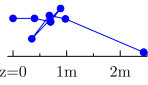
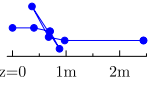
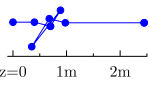
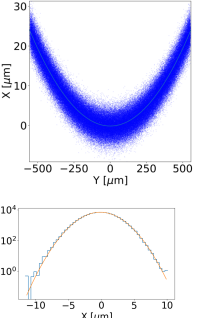
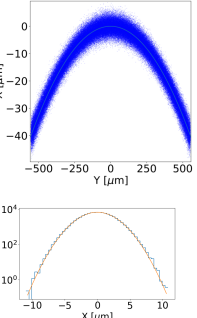
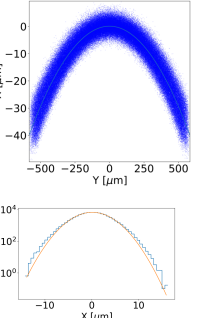
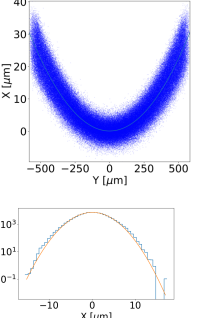
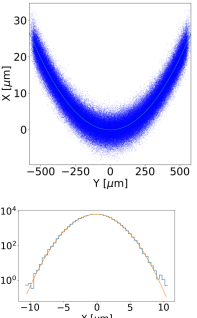
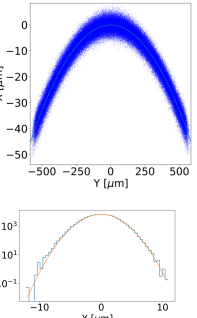
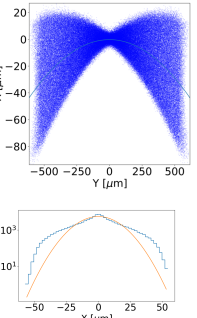
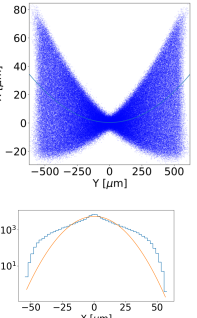
Focusing mirrors certainly may feature a significantly larger aperture; however, would they be also able to produce aberration-free IXS images?

#### IV. IXS IMAGING WITH MIRRORS

Unlike paraboloidal lenses, curved grazing incidence mirrors are in general not good x-ray imaging devices. Some particular combinations of two or more reflectors may comply with the Abbe sine condition and perform as good imaging systems. A prominent example is the Wolter-type mirror pairs [10, 11]. The two mirrors that play the role of collimating and focusing elements in the refocusing system of the x-ray echo spectrometer with the dispersing system in between may perform similarly to a Wolter-type imaging system. In particular, a paraboloidal double-mirror system in a collimating-plus-focusing configuration has the great advantage of producing parallel x-rays between the two reflections, which is perfect for the proper performance of a plane dispersive system (“diffraction grating”) inserted in between [25]. The Abbe sine condition is perfectly fulfilled for the 1:1 1D-imaging case with no dispersing element in between [6]. However, the question still remains open whether perfect imaging can be achieved if a dispersing system is included, and whether this is valid in the 2D case, as x-ray echo spectrometers require.

We study in this section IXS imaging with three different grazing incidence mirror systems composed of (i) two 2D paraboloidal mirrors [20], (ii) two Kirkpatrick-Baez (KB) systems [21] each formed by cylindric parabolic mirrors, and (iii) two Montel [22] systems, made as well of cylindric parabolic mirrors.

TABLE II: Beam cross sections in image plane 2 calculated for the elastic scattering case  $\varepsilon = 0$  for the refocusing system of the x-ray echo spectrometer in four different mirror-crystal configurations with paraboloidal mirrors as collimating and focusing elements. Two cases of the angular apertures  $\Upsilon_v \times \Upsilon_h$  are considered. Numerical values are provided for the vertical image size  $\Delta\tilde{X}_2$  in image plane 2, reduced image size  $\Delta\tilde{x}_2$ , and the spectral resolution  $\Delta\tilde{\varepsilon}$ . The configuration graphs show side views of the beam trajectories (optical axes). The numbers in square brackets correspond to calculations with the horizontal angular aperture increased to  $\Upsilon_h = 10$  mrad. The numbers highlighted in gray correspond to best imaging cases.

Configurations	I	II	III	IV
	 $z=0 \quad 1m \quad 2m$ $(- \pi-, \pi-, \pi+, 0+ -)$ $G_D < 0$	 $z=0 \quad 1m \quad 2m$ $(- \pi+, \pi+, \pi-, 0- -)$ $G_D > 0$	 $z=0 \quad 1m \quad 2m$ $(- \pi-, \pi-, \pi+, 0+ +)$ $G_D < 0$	 $z=0 \quad 1m \quad 2m$ $(- \pi+, \pi+, \pi-, 0- +)$ $G_D > 0$
$\Upsilon_v = 1.5$ mrad $\Upsilon_h = 1.5$ mrad				
$\Upsilon_v = 1.5$ mrad $\Upsilon_h = 10$ mrad				
$\Delta\tilde{X}_2$ [ $\mu\text{m}$ ]	24.29 $\pm$ 0.04 [26.9 $\pm$ 0.1]	40.73 $\pm$ 0.08 [45.03 $\pm$ 0.2]	40.1 $\pm$ 0.2 [44.0 $\pm$ 0.6]	30.55 $\pm$ 0.09 [34.1 $\pm$ 0.5]
$\Delta\tilde{x}_2$ [ $\mu\text{m}$ ]	5.28 $\pm$ 0.01 [5.28 $\pm$ 0.01]	5.43 $\pm$ 0.01 [5.42 $\pm$ 0.01]	7.58 $\pm$ 0.02 [29.1 $\pm$ 0.1]	7.56 $\pm$ 0.01 [29.1 $\pm$ 0.1]
$\Delta\tilde{\varepsilon}$ [ $\mu\text{eV}$ ]	105.5 $\pm$ 0.3 [105.5 $\pm$ 0.3]	108.7 $\pm$ 0.3 [108.4 $\pm$ 0.2]	151.6 $\pm$ 0.4 [583 $\pm$ 2]	151.3 $\pm$ 0.3 [583 $\pm$ 2]

### A. Elastic scattering $\varepsilon = 0$

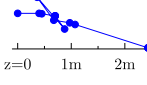
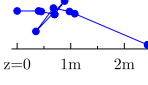
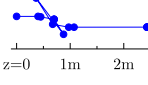
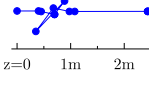
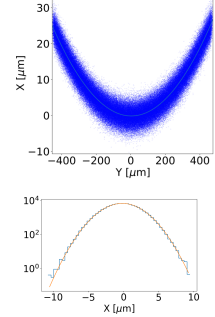
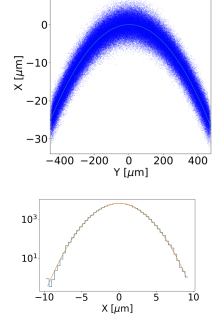
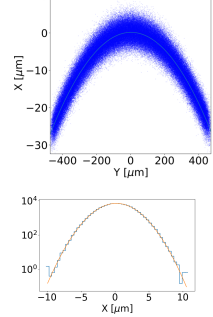
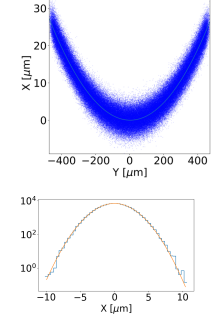
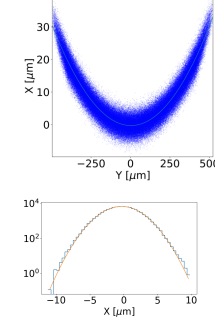
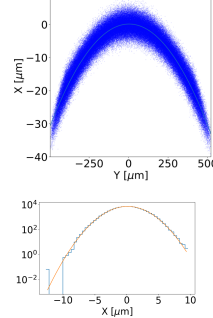
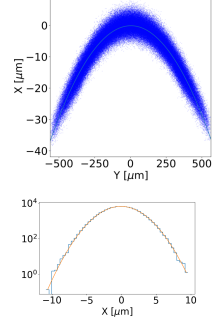
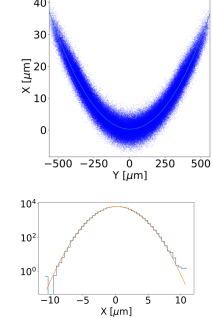
We start with the refocusing system composed of two 2D paraboloidal mirrors and the CDDW dispersing element in between. The setting of the two paraboloids is not unique. They can be in a parallel or antiparallel configuration. Extending the nomenclature used for crystal systems, we can label these mirror configurations as  $(-||+)$  and  $(-||-)$ , respectively. Here, plus corresponds to the x-ray beam reflected counterclockwise from an optical element, and minus clockwise. Importantly, the relative position of the CDDW system must be properly chosen to match the sign of the linear dispersion rate  $G_D$  on the sample in reference plane 1 [the first crystal may reflect counterclockwise (+) or clockwise (-)], which is critical to obeying the refocusing condition Eq. (1).

Table II shows graphs of four possible unique mirror-crystal configurations fulfilling the refocusing condition. Each configuration is coded by a sequence of signs. The left and right outer signs correspond to mirrors  $F_1$  and  $F_2$ , respectively. The crystals are additionally characterized by the azimuthal angles of incidence  $\pi$  or 0, see [1, 6] for details. Configurations with all signs reversed including the  $G_D$  sign represent four equivalent configurations.

Table II presents results of the ray tracing simulations: the images and the reduced image profiles (similar to those in Fig. 3(a)-(e)). The simulations are performed for two different angular apertures:  $\Upsilon_v = \Upsilon_h = 1.5$  mrad (nominal case of the  $0.07 \text{ nm}^{-1}$  momentum transfer resolution) and  $\Upsilon_v = 1.5$  mrad;  $\Upsilon_h = 10$  mrad (a larger horizontal aperture). Table II also provides calculated values of the vertical image size  $\Delta\tilde{X}_2$ , the reduced image size  $\Delta\tilde{x}_2$ , and of the spectral resolution  $\Delta\tilde{\varepsilon}$ .



TABLE III: Similar to Table II, however, with the results calculated for KB-mirror systems as collimating and focusing elements.

Configurations	I  $(- \pi-, \pi-, \pi+, 0+ -)$ $G_D < 0$	II  $(- \pi+, \pi+, \pi-, 0- -)$ $G_D > 0$	III  $(- \pi-, \pi-, \pi+, 0+ +)$ $G_D < 0$	IV  $(- \pi+, \pi+, \pi-, 0- +)$ $G_D > 0$
$\Upsilon_v = 1.5$ mrad $\Upsilon_h = 1.5$ mrad				
$\Upsilon_v = 1.5$ mrad $\Upsilon_h = 10$ mrad				
$\Delta\tilde{X}_2$ [ $\mu\text{m}$ ]	$26.92 \pm 0.02$ [33.32 $\pm$ 0.02]	$26.88 \pm 0.02$ [33.18 $\pm$ 0.02]	$27.16 \pm 0.02$ [36.77 $\pm$ 0.02]	$27.19 \pm 0.02$ [36.88 $\pm$ 0.03]
$\Delta\tilde{x}_2$ [ $\mu\text{m}$ ]	$5.11 \pm 0.01$ [5.35 $\pm$ 0.01]	$5.11 \pm 0.01$ [5.34 $\pm$ 0.01]	$5.13 \pm 0.01$ [5.35 $\pm$ 0.01]	$5.13 \pm 0.01$ [5.34 $\pm$ 0.01]
$\Delta\tilde{\varepsilon}$ [ $\mu\text{eV}$ ]	$102.2 \pm 0.2$ [107.0 $\pm$ 0.2]	$102.1 \pm 0.3$ [106.8 $\pm$ 0.3]	$102.7 \pm 0.2$ [107.0 $\pm$ 0.1]	$102.6 \pm 0.2$ [106.8 $\pm$ 0.2]

Only the  $(-||-)$  mirror configurations I and II result in sharp reduced images with Gaussian profiles and image sizes of  $\Delta\tilde{x}_2 \simeq 5 \mu\text{m}$  in agreement with those expected from the paraxial theory value of  $\Delta x_2 = 5 \mu\text{m}$ , both for  $\Upsilon_h=1.5$  mrad and 10 mrad. The imaging properties of systems III and IV are worse but still almost as good for  $\Upsilon_h=1.5$  mrad. However, major aberrations explode with increasing the horizontal angular aperture to 10 mrad. According to Table II results, configuration I is the best, providing the smallest image size  $\Delta\tilde{X}_2$ , the smallest reduced image size  $\Delta\tilde{x}_2$ , and therefore the best spectral resolution  $\Delta\tilde{\varepsilon}$ , in agreement with the design value and with the lens case.

Table III shows results of similar calculations for the refocusing system, in which the two paraboloidal mirrors are replaced by two KB-mirror systems. The vertical focusing mirrors (VFM) are placed as the paraboloidal mirrors at distances  $f_1$  and  $f_2$  from reference planes 1 and 2, respectively, while the horizontal focusing mirrors (HFM) are at 50 mm and 100 mm downstream the VFMs, respectively, with the focal lengths of the HFMs appropriately corrected. Remarkably, the refocusing system composed

of the KB-mirror systems produce sharp images in all four possible configurations (as the paraboloidal mirrors in the best configuration I).

The refocusing system comprising Montel mirrors performs in all four possible configurations very similar to the KB-mirror case, provided the  $\Upsilon_h=1.5$ -mrad angular aperture case is considered (see Table VII of Appendix B). However, the Montel mirrors are more sensitive to the horizontal divergence, producing significantly worse results in the  $\Upsilon_h=10$ -mrad angular aperture case especially in configurations I and IV. The better performance of the KB-mirror compared to the Montel-mirror systems maybe due to the fact that the VFM and HFM in the KB case are perfectly aligned along the optical axis (x-ray trajectory). In contrast, VFM and HFM are orthogonal to each other in the Montel case, composing a system with an ill-defined optical axis.

The performance of the refocusing systems composed of KB mirrors appears to be also least sensitive to increasing the vertical angular aperture  $\Upsilon_v$  as the results of the calculations of the reduced image size  $\Delta\tilde{x}_2$  and of the spectral resolution  $\Delta\tilde{\varepsilon}$  show, presented in Table IV.

TABLE IV: Reduced vertical image size  $\Delta\tilde{x}_2$  [ $\mu\text{m}$ ] in reference plane 2 as a function of  $\Upsilon_v$  (with a fixed  $\Upsilon_h=1.5$  mrad) calculated for paraboloidal, KB, and Montel mirror systems in configuration I. Values are shown for the elastic scattering case ( $\varepsilon = 0$ ) and for the inelastic case  $\varepsilon = 4$  meV in brackets (see Section IV B 2 for details). Note that  $\Delta\tilde{x}_2 = 5 \mu\text{m}$  corresponds to a spectral resolution of  $\Delta\varepsilon=0.1$  meV.

$\Upsilon_v$ mrad	Paraboloids	KBs	Montel
1.5	5.3 (5.4)	5.1 (5.1)	5.7 (5.5)
3.0	6.0 (6.5)	5.5 (5.5)	6.9 (6.5)
6.0	7.8 (8.8)	6.6 (6.6)	9.8 (8.6)
12.0	11.3 (13.8)	9.1 (9.1)	15.1 (13.2)
24.0	18.6 (26.3)	13.8 (14.3)	

The image size and spectral resolution degrade roughly by a factor of two from  $\Delta\varepsilon=0.1$  meV to  $\simeq 0.2$  meV with increasing  $\Upsilon_v$  from the nominal 1.5 mrad to 10 mrad. Note that the calculations are performed with mirrors and crystals long enough to accept the full beam.

In summary, in the elastic scattering case, the refocusing systems composed of focusing mirrors perform in the best mirror-crystal configurations very similarly to the systems composed of lenses. Whether this is still true for the inelastic scattering case, we study in the next section.

## B. Inelastic scattering $\varepsilon \neq 0$

### 1. Aberrations in the image plane

In the case of lenses, the reduced image size in reference plane 2 does not change if inelastic scattering ( $\varepsilon \neq 0$ ) takes place. This is no longer the case if mirrors are used instead of lenses. Indeed, the reduced image size in reference plane 2 plotted versus  $\varepsilon$  in Fig. 5 appears to grow quadratically with  $\varepsilon$ :  $\Delta\tilde{x}_2(\varepsilon) - \Delta\tilde{x}_2(0) \propto \varepsilon^2$ . Thus the mirror systems behave very differently compared to the lens systems: the spectral resolution degrades with  $|\varepsilon|$ . This degradation can be reduced or even eliminated if the vertical angular aperture  $\Upsilon_v$  is diminished substantially by a factor 10 or 100. This, however, would reduce the photon flux in the detector to unacceptably low values. Interestingly, the horizontal angular aperture does not have the same effect, except for Montel mirror systems, which are very sensitive to large  $\Upsilon_h$ .

The different behavior of the mirror- and lens-based systems could be related to focusing element  $F_2$ . While collimating element  $F_1$  functions in the same way both in the elastic and inelastic scattering regimes, see Figs. 1(v<sub>e</sub>)-(v<sub>i</sub>). In contrast, it is not the case for focusing element  $F_2$ , as the incidence angle changes with  $\varepsilon$  for it. This is probably of no significance if lenses are used as  $F_2$ , for which the incidence angle is close to normal. This appeared to be important if grazing incidence mirrors are used instead. However, the studies, which are discussed in Appendix B and in Fig. 13, show that

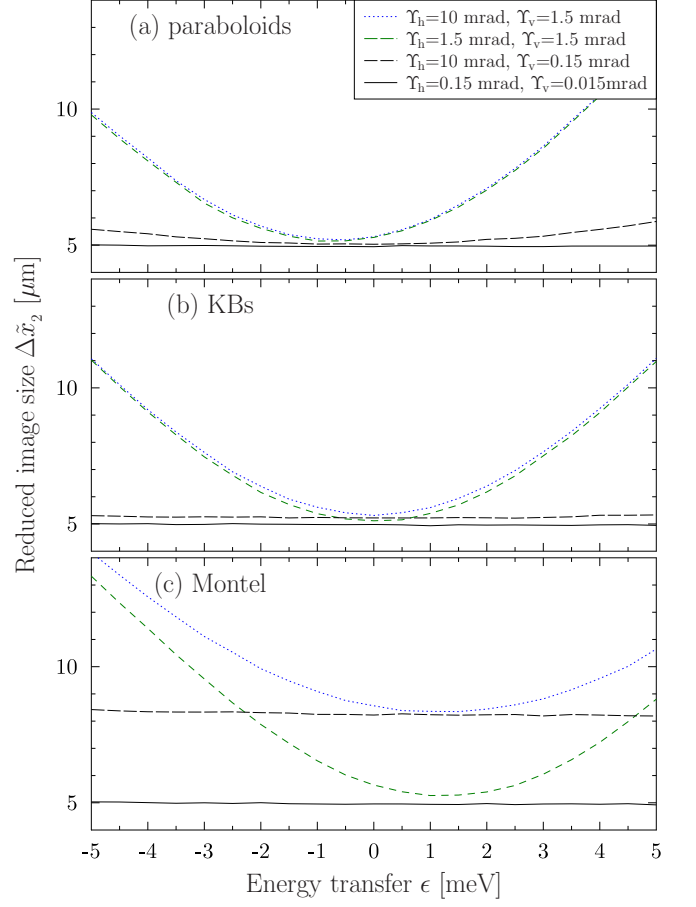


FIG. 5: Reduced vertical image size  $\Delta\tilde{x}_2$  in reference plane 2 as a function of the energy transfer  $\varepsilon$ , calculated for the refocusing system with (a) the paraboloidal mirrors (b) KB-mirror systems, and (c) Montel systems, all in configuration I (see Table II) for different values of the angular apertures  $\Upsilon_h$  and  $\Upsilon_v$ .

no optimal  $f_2$  value can be found in any of the considered mirror cases, which would eliminate or mitigate the degradation of the spectral resolution with  $\varepsilon$ . They show, though, that the 1:1 imaging is preferred to be least sensitive to spectral resolution degradation by large angular apertures  $\Upsilon_v$  and  $\Upsilon_h$ .

### 2. Defocus correction in an oblique image plane

In this section we show that the degradation of the reduced vertical size when passing from elastic ( $\varepsilon = 0$ ) to inelastic ( $\varepsilon \neq 0$ ) scattering is merely the defocus aberration that can be easily compensated.

For this, we calculate how the reduced image size changes along the optical axis for different values of  $\varepsilon$ . The results presented in Fig. 6 show that the smallest reduced image size (waist) for any  $\varepsilon$  is in fact equal to the elastic image size  $\Delta\tilde{x}_2(\varepsilon = 0)$ . However, it is attained with a shift  $z_2(\varepsilon) - z_2(0)$  along the optical axis

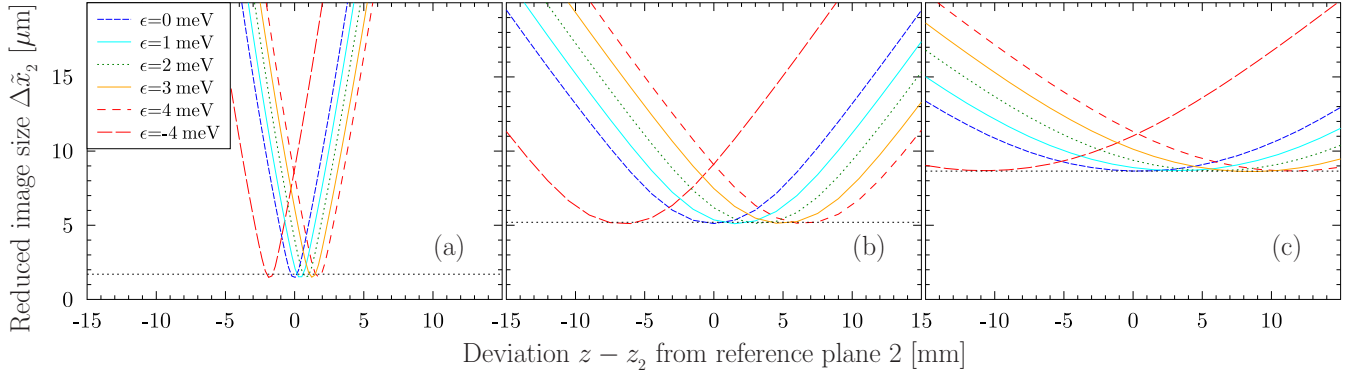


FIG. 6: Reduced vertical image size  $\Delta\tilde{x}_2$  as a function of deviation  $z - z_2$  from reference image plane 2, calculated for different energy transfer values  $\varepsilon$  and for selected focal length values  $f_2$  of imaging mirror  $F_2$ : (a)  $f_2 = 0.4$  m, (b)  $f_2 = 1.471$  m, and (c)  $f_2 = 2.5$  m. Calculations are for the KB-mirrors case in mirror-crystal configuration I (see Table III), and for the angular apertures  $\Upsilon_v = \Upsilon_v = 1.5$  mrad. See Fig. 14 of Appendix B for the similar results of the paraboloidal or Montel-mirror systems.

from the location  $z_2$  of the nominal image plane.<sup>2</sup> The waist size scales with the focal length  $f_2$  in Figs. 6(a), (b), and (c), because it changes the magnification factor  $A_R = -b_{U_R} f_2 / f_1$ , Eq. (5).

The waist position shifts linearly with  $\varepsilon$  as  $z_2(\varepsilon) - z_2(0) = \varepsilon / \gamma$ , see Fig. 7. The slope  $\gamma$  depends on focal length  $f_2$  of mirror  $F_2$  and on mirrors' incidence angle  $\varphi$ , as illustrated in Figs. 7(a) and (b), respectively. The slope  $\gamma$  is independent of the CDDW-to- $F_2$  distance (the results of calculations are not shown).

The loci of the waists is therefore a line inclined to the optical  $z$ -axis by an angle  $\psi = G_R \gamma$ . In particular, if  $f_2 = 1.471$  m, which corresponds to the 1:1 imaging, the inclination of the IXS image plane is  $\psi \simeq \varphi$ , see numerical values in the inset of Fig. 7(b). In a more general case,  $\psi$  is still proportional to  $\varphi$  but scales with the magnification factor of the refocusing system as  $\psi \simeq \varphi (b_{U_R} f_2 / f_1)$ , see values in the inset of Fig. 7(a).

The spectral resolution degradation in the nominal image plane 2, see Fig. 5, therefore can be compensated by inclination of the x-ray pixel detector by the angle  $\psi$ . Such an inclination may simultaneously improve the detector's spatial resolution.<sup>3</sup> For example, if the detector has a pixel size  $p = 50$   $\mu\text{m}$ , its projection on reference plane 2 and thus the spatial resolution becomes  $p\psi \simeq 1.5$   $\mu\text{m}$  (for  $\psi = 30$ -mrad) or  $p\psi \simeq 1.3$   $\mu\text{m}$  (for

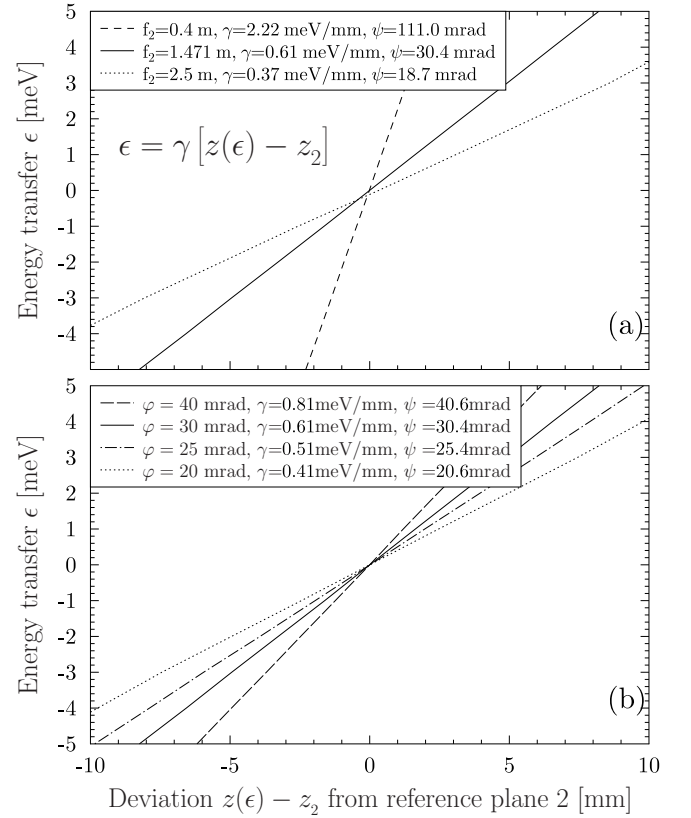


FIG. 7: Correspondence between the energy transfer  $\varepsilon$  and the deviation  $z(\varepsilon) - z_2$  from reference plane 2 of the reduced image with the smallest size (waist). Calculated for the KB-mirrors case. (a) Derived from data in Fig. 6 for selected focal length values  $f_2$ . Mirrors' incidence angle is  $\varphi = 30$  mrad, and angular apertures  $\Upsilon_v = \Upsilon_h = 1.5$  mrad. (b) Calculated with  $f_2 = 1.471$  m (1:1 imaging) and selected values of glancing angle of incidence  $\varphi$ . See Fig. 15 of Appendix B for the results of the paraboloidal or Montel-mirror systems.

<sup>2</sup> At the first glance, the beam size dependences in Fig. 6 may produce an impression that the vertical beam size changes with  $z$  as

$$\Delta\tilde{x}_2(z, \varepsilon) = \Delta\tilde{x}_2(0) \sqrt{1 + [(z - z_2(\varepsilon))/z_R]^2} \quad (9)$$

for any  $\varepsilon$ , i.e., as the Gaussian beam size would change with a waist size of  $\Delta\tilde{x}_2(0)$  and Rayleigh range  $z_R$  [26, 27]. However, this is not the case, because numerical simulations reveal a quadratic component at large  $z$ .

<sup>3</sup> A similar approach is used in soft x-ray grating spectrometers, see, e.g., [28]

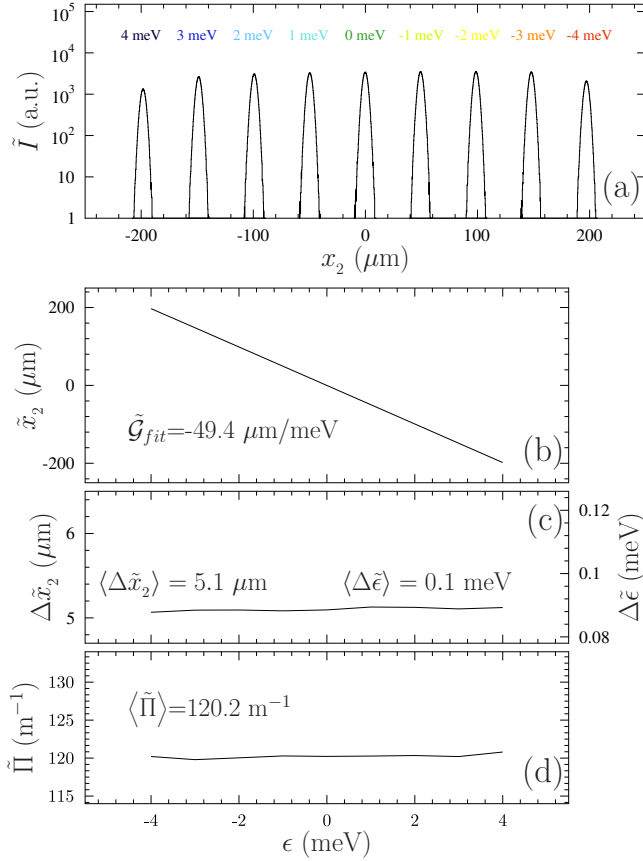


FIG. 8: Performance characteristics of the x-ray echo spectrometer with the refocusing system composed of KB mirrors. IXS spectra are imaged on the oblique image plane. Compare with the results of Fig. 4 presented for the case of lenses as the focusing elements, and with the results for the paraboloidal or Montel-mirror systems in Fig. 16 of Appendix B.

$\psi = 25\text{-mrad}$ ).<sup>4</sup>

Figure 8 summarizes IXS imaging properties of the refocusing system composed of grazing incidence curved KB-mirror systems and the pixel x-ray detector in the oblique image plane. The properties are very similar to those of the system composed of paraboloidal lenses. The only difference is that the aberration-free imaging takes place in the oblique image plane at the angle  $\psi$  to the optical axis. The imaging properties of the refocusing system composed of the paraboloidal or Montel-mirror

TABLE V: Reduced image size (in  $\mu\text{m}$ ) in the refocusing system of the x-ray echo spectrometer comprising mirror systems with different glancing angles of incidence  $\varphi$ .

Mirror type / $\varphi$ [mrad]	20	25	30	40
KB	5.29	5.17	5.10	5.05
Paraboloids	5.54	5.38	5.27	5.15

systems are very similar and presented in Fig. 14 of Appendix B. A slightly better resolution is found for KBs than for paraboloids and Montel systems.

### C. Effect of glancing angle of incidence

Typically, the imaging property of a solitary mirror degrades with decreasing glancing angle of incidence because of the illumination of an increasing part of the optic. Here we study the effect of glancing angle of incidence  $\varphi$  on the imaging properties of the refocusing system composed of mirror pairs and the CDDW dispersing element in between.

Table V presents results of calculations of the image size in case of KB and paraboloidal systems for selected values of  $\varphi$ . They show that the image size slightly increases and therefore the spectrometer resolution degrades when glancing angle decreases. The output intensity remains constant if mirrors are used long enough to accept the whole beam (data not shown). This means that larger  $\varphi$  values are preferred. However, other considerations speak against large  $\varphi$ . Larger  $\varphi$  requires multilayer coatings with smaller periods and eventually smaller reflectivity. Glancing angle of incidence  $\varphi \simeq 30$  mrad is optimal for present-day technology, and therefore are used in the current simulations.

### D. Effect of slope errors

Mirrors' slope errors will surely contribute to broadening the reduced image size and degrading the spectrometer's spectral resolution. It is therefore important to determine the admissible values for the slope errors.

Figure 9 presents results of the ray tracing calculations for reduced image profiles by the refocusing system composed of paraboloidal mirror pairs for selected values of slope errors: 0, 0.5, 1, and 2.5  $\mu\text{rad}$  (rms), same for both mirrors. They show a rapid degradation of the reduced image size and signal strength with increasing slope errors, and indicate that the slope errors of the mirrors must stay below 0.5  $\mu\text{rad}$  in the present case.

These results can be supported and understood by simple analytical considerations,<sup>5</sup> which in particular show

<sup>4</sup> To be practical, the application of a high- $Z$  sensor material is required with a photo-absorption length  $L_a \ll p$ . A CdTe  $50 \times 50\text{-}\mu\text{m}^2$  pixel detector would be most optimal for this application. CdTe:  $L_a = 6.5 \mu\text{m}$  for 9.1 keV photons,  $L_a = 11.4 \mu\text{m}$  for 11.210 keV photons,  $L_a = 22.9 \mu\text{m}$  for 14.41 keV. To image a beam with a  $400\text{-}\mu\text{m}$  large vertical size (corresponds to a 8-meV spectral window of imaging), a 12.5-mm CdTe sensor would be required. Photon-counting pixel detectors with such sensors are state of the art [29].

<sup>5</sup> Slope error  $\xi$  of a mirror with a focal length  $f$  results in additional

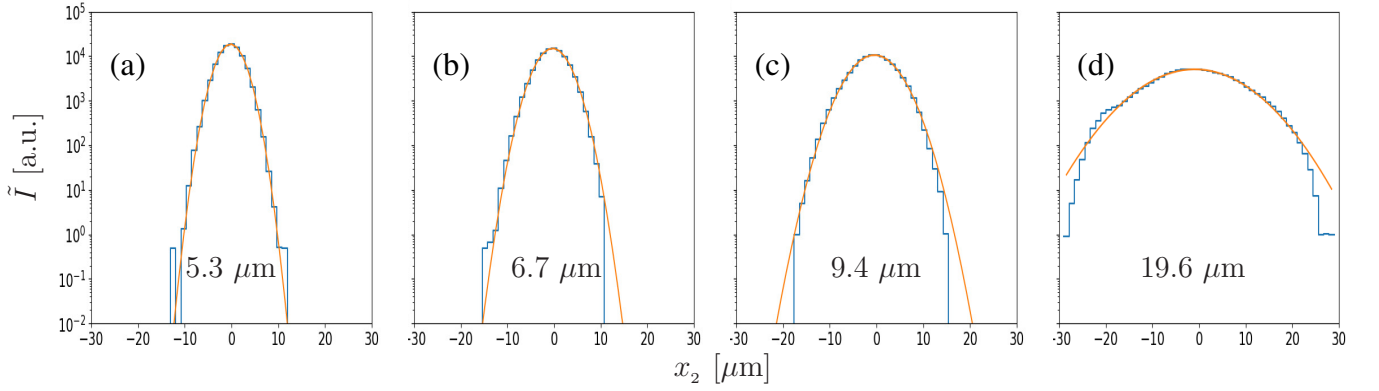


FIG. 9: Reduced image profiles in elastic scattering ( $\varepsilon = 0$ ) for paraboloidal mirrors with different slope errors: (a) 0, (b) 0.5, (c) 1.0, and (d) 2.5  $\mu\text{rad}$  (rms), respectively. The corresponding image size widths  $\Delta\tilde{x}_2$  (FWHM) are displayed in the graphs.

that it is mirror  $F_2$  with the largest focal length  $f_2$  that is the critical optic requiring such a small slope error value. Therefore, using mirrors with smaller focal lengths is preferable from this point of view.

## V. IMAGING IXS SPECTRA OF “GLYCEROL”

Finally, in this section we study the ability of the x-ray echo spectrometer to image IXS spectra of real samples. As an example, we select a liquid sample with properties closely resembling glycerol at room temperature.

The IXS spectra in liquids are typically modeled by the normalized dynamical structure factor

$$\frac{S(Q, \varepsilon)}{S(Q)} = f_Q \delta(\varepsilon) + \frac{1 - f_Q}{\pi} \frac{\Gamma_Q \Omega_Q^2}{(\varepsilon^2 - \Omega_Q^2)^2 + \varepsilon^2 \Gamma_Q^2}, \quad (10)$$

$$\Omega_Q = v_s \hbar Q, \quad \Gamma_Q = BQ^2, \quad (11)$$

which is a sum of the delta function for the elastic component and the damped harmonic oscillator for the inelastic component measured at selected momentum transfer  $Q$  [30]. The sound velocity  $v_s = 2.8 \text{ km/s}$ , reduced broadening  $B = 3 \text{ nm}^2 \text{ meV}$ , and the elastic line fraction  $f_Q = 0.7$  are assumed to be constant for simplicity, i.e.,  $Q$ -independent, which is in fact not necessarily the case in practice. This assumption represents merely an interpolation of the known data for glycerol liquid [31, 32] into

the yet unexplored range of  $Q \lesssim 0.5 \text{ nm}^{-1}$ . The graphs in the lower row of Fig. 10 show in red the normalized dynamical structure factor  $S(Q, \varepsilon)/S(Q)$  of the “glycerol” calculated for selected  $Q$  values using Eqs. (10)-(11). The elastic line in green is a Gaussian with FWHM of 0.1-meV – equivalent to the resolution function of the x-ray echo spectrometer.

In the simulations presented in the previous sections, the sample introduced a constant energy transfer  $\varepsilon$  ( $\varepsilon=0$  for elastic and  $\varepsilon \neq 0$  for inelastic cases). Now, each ray will be affected by a random  $\varepsilon$  sampled by  $S(Q, \varepsilon)/S(Q)$ , thus simulating the real effect of the photon energy change by the sample with a probability determined by the ideal IXS spectrum of Eq. (10).

The real IXS spectra measured in experiments represent a convolution of  $S(Q, \varepsilon)/S(Q)$  with the instrumental function. This convolution is naturally included in the ray tracing simulations. The graphs in the upper row of Fig. 10 present the “glycerol” IXS spectra obtained by the ray tracing through the refocusing system of the x-ray echo spectrometer equipped with the ideal lenses. The system equipped with the paraboloidal mirrors produces almost identical results (not shown). However, in the latter case, the detector plane has to be inclined by an angle of  $\varphi = 30.5 \text{ mrad}$  with the optical axis. Recall that the spatial image produced in the detector is reduced by removing the parabola calculated for the elastic scattering with parameters provided in Fig. 4 for the lenses and in Fig. 8 for KB-mirror systems.

The ray tracing results practically reproduce the spectral features of  $S(Q, \varepsilon)/S(Q)$  for  $Q=0.5 \text{ nm}^{-1}$  and  $Q=0.25 \text{ nm}^{-1}$ . The phonon peaks are also well resolved in the  $Q=0.1 \text{ nm}^{-1}$  case, however, they appear blurred because the phonon lines are already narrower than the resolution function. The example of the presented simulations confirms that x-ray echo spectrometers are capable of aberration-free imaging IXS spectra.

---

relative broadening  $\mu = 2\xi f/\Delta x$  of the image size  $\Delta x$ . For the resultant image size  $\Delta x\sqrt{1+\mu^2}$  to be not increased by more than 10%, the relative broadening should be  $\mu \lesssim \sqrt{0.2} = 0.46$  and the slope errors  $\xi \lesssim \mu\Delta x/2f$ . Assuming  $\Delta x = 5 \mu\text{m}$  (FWHM) or  $\Delta x = 2.13 \mu\text{m}$  (rms), we obtain  $\xi_1 \lesssim 1.2 \mu\text{rad}$  (rms) for a mirror with  $f_1 = 0.4 \text{ m}$  and  $\xi_2 \lesssim 0.33 \mu\text{rad}$  (rms) for a mirror with  $f_2 = 1.471 \text{ m}$ . If a 20% broadening is admissible, then  $m = 0.66$ , and the corresponding admissible slope errors are  $\xi_1 \lesssim 1.76 \mu\text{rad}$  (rms) and  $\xi_2 \lesssim 0.5 \mu\text{rad}$  (rms).



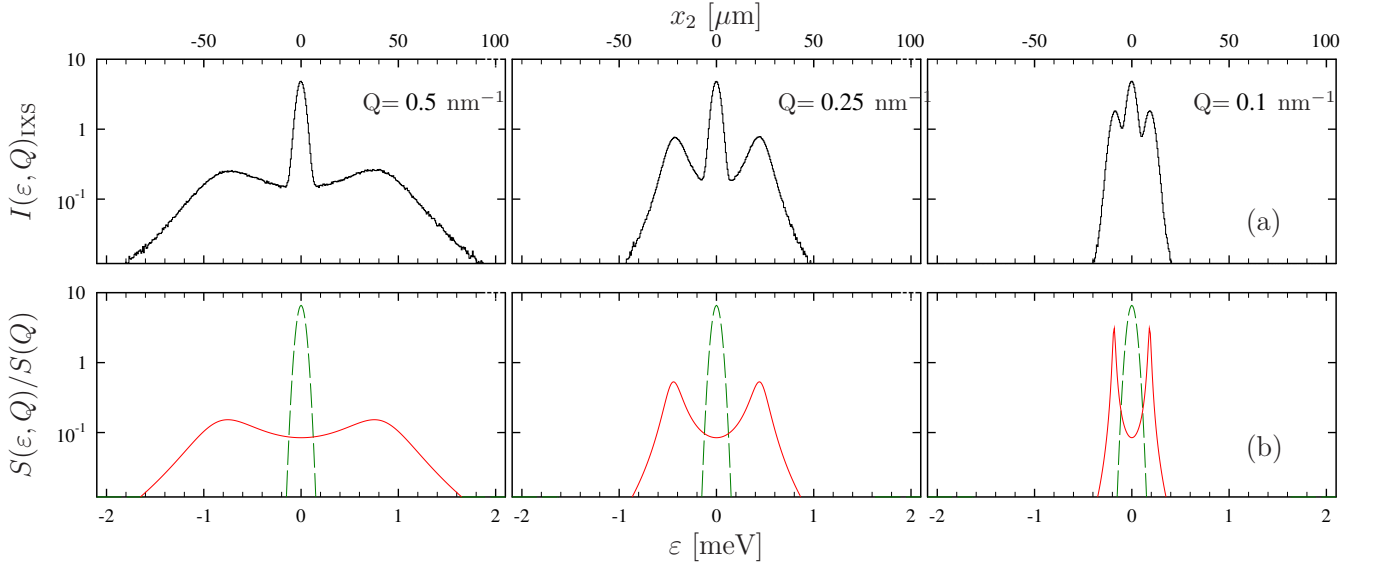


FIG. 10: IXS spectra of “glycerol” liquid at selected momentum transfer values  $Q$ . Upper row: IXS spectra  $I(\varepsilon, Q)_{\text{IXS}}$  obtained by ray tracing through the refocusing system of the 0.1-meV-resolution x-ray echo spectrometer composed of ideal lenses. The system with paraboloidal mirrors produces almost identical results provided the IXS spectra are imaged on the oblique plane. Lower row: the normalized dynamical structure factor  $S(\varepsilon, Q)/S(Q)$  used in the ray tracing simulations is calculated with Eqs. (10)-(11) and is shown by red solid line. The elastic line in green (dashed line) is a Gaussian with FWHM of 0.1-meV - equivalent to the resolution function of the x-ray echo spectrometer.

## VI. CONCLUSIONS

We have studied conditions for aberration-free imaging of IXS spectra with x-ray echo spectrometers. Aberration-free imaging is essential for achieving high-resolution high-contrast instrumental functions. Numerical ray tracing was applied to a particular case of a 0.1-meV-resolution echo-type IXS spectrometer operating with 9-keV x-rays.

X rays from a Gaussian polychromatic source being dispersed and therefore defocused on the scattering sample by the defocusing system are refocused in the image plane of the refocusing system into a sharp image. The image shifts transversely in the dispersion plane by an amount proportional to inelastic scattering energy transfer  $\varepsilon$ , thus ensuring imaging of IXS spectra.

The images are laterally curved. However, the curvature is spectrometer-invariant, determined by the parameters of the Bragg reflecting crystals of the dispersing element and the focal distances of the focusing elements. The curved images of all elastic and inelastic components can therefore be reduced to flat images. The reduced images reveal Gaussian profiles, if flawless optical elements are in use.

We show that all  $\varepsilon$ -components of IXS spectra are imaged aberration-free, featuring Gaussian profiles of constant width, provided the collimating and focusing optics of the refocusing system of the x-ray echo spectrometer are composed of lenses.

If curved grazing-incidence mirror systems are used instead (paraboloidal, parabolic KB, or parabolic Montel),

the images of all  $\varepsilon$ -components still can be Gaussian and sharp when recorded on the detector plane tilted with respect to the optical axis. The inclination of this oblique image plane to the optical axis is equal to the grazing angle of incidence, in case of 1:1 imaging by the refocusing system. Compensation of the defocus aberration by inclining the x-ray imaging pixel detector simultaneously improves detector’s spatial resolution.

The refocusing system of the 0.1-meV-resolution x-ray echo spectrometer may feature sharp aberration-free images of IXS spectra using any considered mirror type assuming the angular aperture is  $\Upsilon_v = \Upsilon_h = 1.5$  mrad (required by spectrometer’s nominal momentum transfer resolution  $\Delta Q = 0.07 \text{ nm}^{-1}$ ). However, the KB and Montel mirror systems provide sharp images both in the  $(-||-)$  and  $(-||+)$  mirror configurations, while the paraboloidal mirrors work properly only in the  $(-||-)$  configuration. KB-mirror systems appear to be the best imaging devices, as the high image quality by the KB systems is preserved in all configurations also with the horizontal angular aperture increased to  $\Upsilon_h = 10$  mrad. The paraboloidal mirrors can perform similarly, however, only in the 1:1 imaging case in the  $(-||-)$  configuration. The performance of the KB-mirror systems is also least sensitive to the vertical angular aperture  $\Upsilon_v$ .

The instrumental function of echo-type IXS spectrometers has sharp high-contrast Gaussian tails. This is a great advantage over the long Lorentzian tails of the instrumental functions of present-day narrow-band scanning IXS spectrometers [5]. In practice, the contrast of the instrumental function will rely on the quality (small-

ness of the slope errors) of the mirrors of the x-ray echo spectrometers. The simulations show that slope errors better than  $0.5 \mu\text{rad}$  are critical to avoid instrumental function degradation in the 30-mrad grazing incidence mirror case (Fig. 9) with a focal length of  $f_2 = 1.4 \text{ m}$ .

Initial design parameters of the x-ray echo spectrometer derived by analytical ray-tracing theory [6] are in a very good agreement with the results of the numerical simulations. In particular, no meaningful change in the resolution is observed if all the crystals are put at the same position, as the analytical theory assumes.

The results of the studies are applicable also to hard x-ray imaging spectrographs [16], which represent a subsystem of x-ray echo spectrometers. The spectrographs, unlike x-ray echo spectrometers, are dealing with imaging

IXS spectra with a tight non-dispersed monochromatic secondary source on the sample.

The range of applications of the echo-type IXS spectrometers and IXS spectrographs of course includes resonant IXS (RIXS) [33], as a particular case.

## VII. ACKNOWLEDGMENTS

Work at Argonne National Laboratory was supported by the U.S. Department of Energy, Office of Science, Office of Basic Energy Sciences, under contract DE-AC02-06CH11357. Yiones Aouadi is acknowledged for developing a ray tracer for Montel mirrors.

- 
- [1] Yu. Shvyd'ko, Phys. Rev. Lett. **116**, 080801 (2016).
  - [2] F. Mezei, ed., *Neutron Spin Echo.*, vol. 128 of *Lecture Notes in Physics* (Springer, Berlin, 1980).
  - [3] H. S. Fung, C. T. Chen, L. J. Huang, C. H. Chang, S. C. Chung, D. J. Wang, T. C. Tseng, and K. L. Tsang, AIP Conf. Proc. **705**, 655 (2004).
  - [4] C. H. Lai, H. S. Fung, W. B. Wu, H. Y. Huang, H. W. Fu, S. W. Lin, S. W. Huang, C. C. Chiu, D. J. Wang, L. J. Huang, et al., Journal of Synchrotron Radiation **21**, 325 (2014).
  - [5] A. Q. R. Baron, *Synchrotron Light Sources and Free-Electron Lasers* (Springer International Publishing, Switzerland, 2016), chap. "High-Resolution Inelastic X-Ray Scattering", pp. 1643–1757.
  - [6] Yu. Shvyd'ko, Phys. Rev. A **96**, 023804 (2017).
  - [7] A. Suvorov and Y. Q. Cai, Proc. SPIE **9963**, 99630A (2016).
  - [8] O. Chubar and P. Elleaume, EPAC-98 Proceedings pp. 1177–1179 (1998).
  - [9] B. Lengeler, C. Schroer, J. Tümmeler, B. Benner, M. Richwin, A. Snigirev, I. Snigireva, and M. Drakopoulos, J. Synchrotron Radiation **6**, 1153 (1999).
  - [10] H. Wolter, Annalen der Physik **445**, 94 (1952).
  - [11] H. Wolter, Annalen der Physik **445**, 286 (1952).
  - [12] M. Sanchez del Río, N. Canestrari, F. Jiang, and F. Cerrina, Journal of Synchrotron Radiation **18**, 708 (2011).
  - [13] L. Rebuffi and M. Sánchez del Río, Journal of Synchrotron Radiation **23**, 1357 (2016).
  - [14] L. Rebuffi and M. Sánchez del Río, Proc. SPIE **10388**, 103880S (2017).
  - [15] Yu. Shvyd'ko, S. Stoupin, K. Mundboth, and J. Kim, Phys. Rev. A **87**, 043835 (2013).
  - [16] Yu. Shvyd'ko, Phys. Rev. A **91**, 053817 (2015).
  - [17] T. Matsushita and U. Kaminaga, Journal of Applied Crystallography **13**, 465 (1980).
  - [18] M. Sánchez del Río and F. Cerrina, Rev. Sci. Instrum. **63**, 936 (1992).
  - [19] Yu. Shvyd'ko, *X-Ray Optics – High-Energy-Resolution Applications*, vol. 98 of *Optical Sciences* (Springer, Berlin, 2004).
  - [20] H. Yumoto, T. Koyama, S. Matsuyama, Y. Kohmura, K. Yamauchi, T. Ishikawa, and H. Ohashi, Scientific Reports **7**, 16408 (2017).
  - [21] P. Kirkpatrick and A. V. Baez, J. Opt. Soc. Am. **38**, 766 (1948).
  - [22] M. Montel, *X-ray Microscopy and Microradiography* (Academic Press, New York, 1957), chap. X-ray Microscopy with Catamegonic Roof Mirrors, pp. 177–185.
  - [23] K. Mundboth, J. Sutter, D. Laundy, S. Collins, S. Stoupin, and Yu. Shvyd'ko, J. Synchrotron Radiation **21**, 16 (2014).
  - [24] A. Suvorov, D. S. Coburn, A. Cunsolo, J. W. Keister, M. H. Upton, and Y. Q. Cai, J. Synchrotron Radiation **21**, 473 (2014).
  - [25] M. R. Howells, Nuclear Instruments and Methods **177**, 127 (1980).
  - [26] H. Kogelnik and T. Li, Appl. Opt. **5**, 1550 (1966).
  - [27] A. E. Siegman, *Lasers* (University Science Books, Sausalito, California, 1986).
  - [28] G. Ghiringhelli, A. Piazzalunga, C. Dallera, G. Trezzi, L. Braicovich, T. Schmitt, V. N. Strocov, R. Betemps, L. Patthey, X. Wang, et al., Rev. Sci. Instrum. **77**, 113108 (2006).
  - [29] P. Delogu, P. Oliva, R. Bellazzini, A. Brez, P. de Ruvo, M. Minuti, M. Pinchera, G. Spandre, and A. Vincenzi, Journal of Instrumentation **11**, P01015 (2016).
  - [30] G. Monaco, A. Cunsolo, G. Ruocco, and F. Sette, Phys. Rev. E **60**, 5505 (1999).
  - [31] F. Sette, M. H. Krisch, C. Masciovecchio, G. Ruocco, and G. Monaco, Science **280**, 1550 (1998).
  - [32] Yu. Shvyd'ko, S. Stoupin, D. Shu, S. P. Collins, K. Mundboth, J. Sutter, and M. Tolkiehn, Nature Communications **5** (2014).
  - [33] L. J. P. Ament, M. van Veenendaal, T. P. Devereaux, J. P. Hill, and J. van den Brink, Rev. Mod. Phys. **83**, 705 (2011).

## Appendix A: Multi-crystal dispersing elemnts

In this section we show optical schemes, spectral transmission functions, and crystal parameters of the multi-crystal dispersing elements, which were used in the simulations of the x-ray echo spectrometer in this paper. The four-crystal dispersing element of the defocusing system is presented in Fig. 11. The four-crystal dispersing element of the refocusing system is presented in Fig. 12. The crystal parameters for both systems are provided in Table VI.

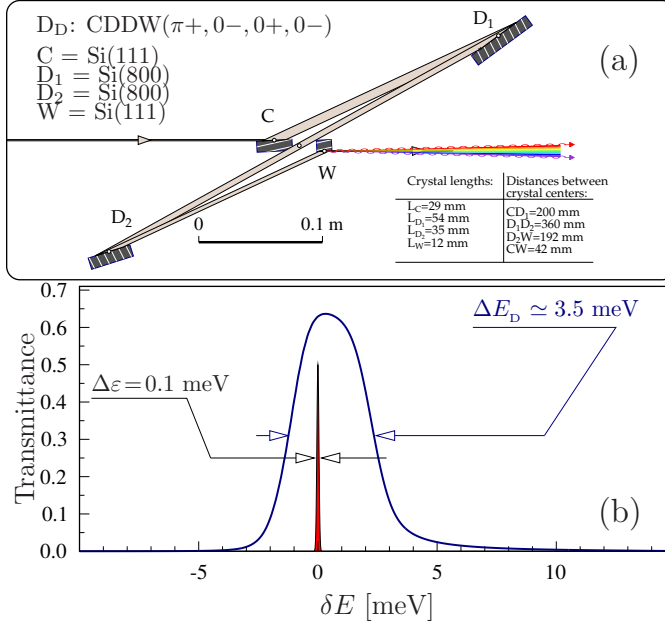


FIG. 11: In-line four-crystal CDDW-type x-ray dispersing element in a  $(\pi+, 0-, 0+, 0-)$  configuration (a) and its spectral transmittance function (b) calculated for the incident beam divergence of  $20 \mu\text{rad}$ . With the crystal parameters provided in [6] and in Table VI of Appendix A, the optic features a spectral transmission function with a  $\Delta E_D = 3.5$  meV bandwidth (b), a cumulative angular dispersion rate  $\mathcal{D}_{U_D} = -32 \mu\text{rad}/\text{meV}$ , and a cumulative asymmetry factor  $b_{U_D} = 2$  appropriate for dispersing element  $D_D$  of the defocusing system  $\hat{O}_D$ . The sharp red line in (b) indicates the 0.1-meV design spectral resolution.

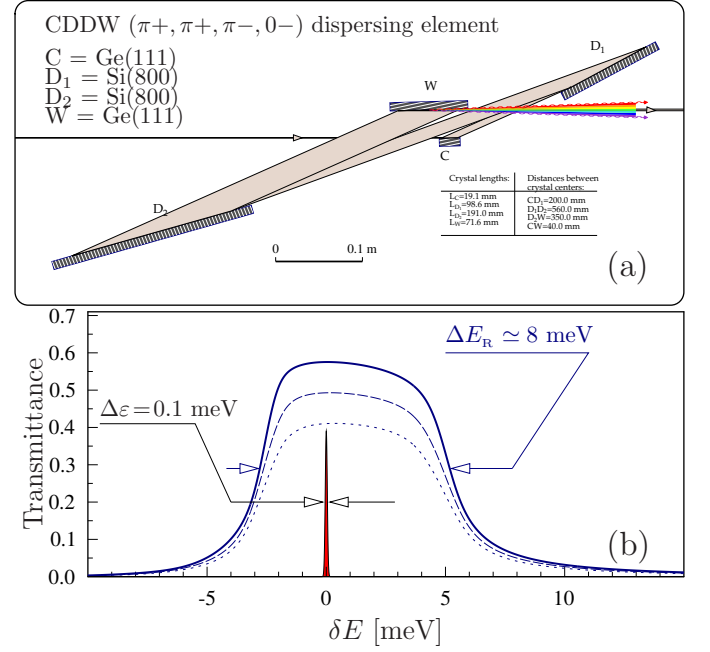


FIG. 12: In-line four-crystal CDDW-type x-ray dispersing element in a  $(\pi+, \pi+, \pi-, 0-)$  scattering configuration (a) and its spectral transmittance function (b) calculated for the incident beam divergence of  $100 \mu\text{rad}$  (bold),  $200 \mu\text{rad}$  (dotted), and  $300 \mu\text{rad}$  (dashed). With the crystal parameters provided in [6] and in Table VI of Appendix A, the optic features a  $\Delta E_R = 8$  meV bandwidth (b), a cumulative angular dispersion rate  $\mathcal{D}_{U_R} = -34.2 \mu\text{rad}/\text{meV}$ , a cumulative asymmetry factor  $b_{U_R} = 0.27$ , and  $\mathcal{D}_{U_R}/b_{U_R} = -125.5 \mu\text{rad}/\text{meV}$ , appropriate for dispersing element  $D_R$  of the refocusing system  $\hat{O}_R$ . The sharp line in (b) presents the 0.1-meV design spectral resolution  $\Delta\epsilon$  of the x-ray echo spectrometer.

crystal element (e)	$\mathbf{H}_e$	$\eta_e$	$\theta_e$	$\Delta E_e^{(s)}$	$\Delta\theta_e^{(s)}$	$b_e$	$s_e \mathcal{D}_e$
[material]	(hkl)	deg	deg	meV	$\mu\text{rad}$		$\frac{\mu\text{rad}}{\text{meV}}$
$D_D$ : CDDW ( $\pi+,0-,0+,0-$ ), Fig. 2							
1 C [Si]	(1 1 1)	-10.5	12.5	1304	32	-0.09	-0.02
2 $D_1$ [Si]	(8 0 0)	77.7	88	27	85	-1.38	-1.19
3 $D_2$ [Si]	(8 0 0)	77.7	88	27	85	-1.38	+1.19
4 W [Si]	(1 1 1)	10.5	12.5	3013	71	-11.2	-0.24
Cumulative values			$\Delta\theta_D$	$\Delta E_D$	$\Delta\theta'_D$	$b_{\cup D}$	$\mathcal{D}_{\cup D}$
			$\mu\text{rad}$	meV	$\mu\text{rad}$		$\frac{\mu\text{rad}}{\text{meV}}$
			57	3.5	112	1.91	-31.7
$D_R$ : CDDW ( $\pi+, \pi+, \pi-, 0-$ ), Fig. 3							
1 C [Ge]	(1 1 1)	-10.5	12.0	3013	71	-0.07	-0.02
2 $D_1$ [Si]	(8 0 0)	-83.75	88	27	85	-0.52	-1.50
3 $D_2$ [Si]	(8 0 0)	-83.75	88	27	85	-0.52	+1.50
4 W [Ge]	(1 1 1)	10.5	12.0	3013	71	-14.75	-0.31
Cumulative values			$\Delta\theta_R$	$\Delta E_R$	$\Delta\theta'_R$	$b_{\cup R}$	$\mathcal{D}_{\cup R}$
			$\mu\text{rad}$	meV	$\mu\text{rad}$		$\frac{\mu\text{rad}}{\text{meV}}$
			262	8	272	0.27	-34.15

TABLE VI: Parameters of the CDDW-type in-line crystal optics designed as dispersing elements  $D_D$ ,  $D_R$  of the defocusing  $\hat{O}_D$  and refocusing  $\hat{O}_R$  systems of the 0.1-meV-resolution x-ray echo spectrometer. For each optic, the table presents crystal elements (e=C,D<sub>1</sub>,D<sub>2</sub>,W) and their Bragg reflection parameters: (hkl), Miller indices of the Bragg diffraction vector  $\mathbf{H}_e$ ;  $\eta_e$ , asymmetry angle;  $\theta_e$ , glancing angle of incidence; Bragg reflection intrinsic spectral width  $\Delta E_e^{(s)}$  and angular acceptance  $\Delta\theta_e^{(s)}$  in symmetric scattering geometry, respectively;  $b_e$ , asymmetry ratio; and  $s_e \mathcal{D}_e$ , angular dispersion rate with deflection sign. For each optic, also shown are: angular acceptance  $\Delta\theta_X$  (X=D,R) and spectral bandwidth  $\Delta E_X$  as derived from the dynamical theory calculations, the angular spread of the dispersion fan  $\Delta\theta'_X = |\mathcal{D}_{\cup X}| \Delta E_X$ , and the cumulative values of the asymmetry parameter  $b_{\cup X}$  and the dispersion rate  $\mathcal{D}_{\cup X}$ . X-ray photon energy is  $E = 9.13708$  keV.

## Appendix B: IXS imaging performance with different mirror systems

Very often the results of the calculations of imaging IXS spectra with different types of mirror systems look similar. Not to overwhelm the main part of the paper with too many details we have moved such data into this appendix, which contains a collection of supplementary tables and figures.

Table VII shows elastic signal imaging with the Montel mirror systems, similar to those shown for the paraboloidal and KB mirror systems in Tables II and III, respectively.

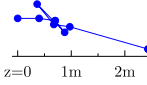
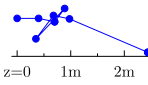
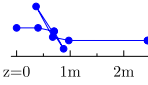
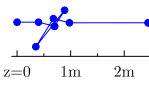
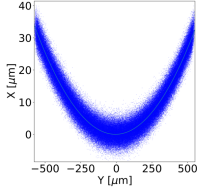
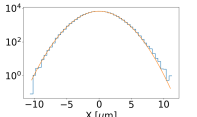
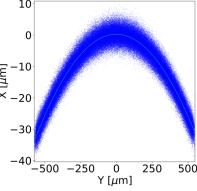
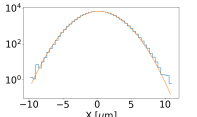
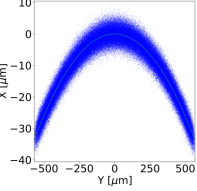
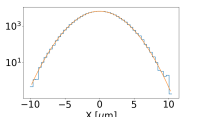
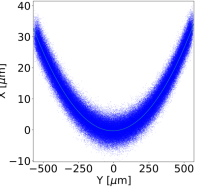
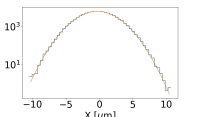
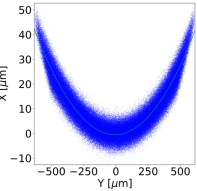
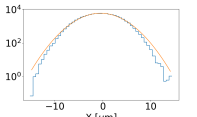
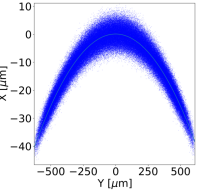
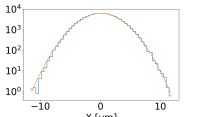
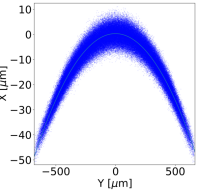
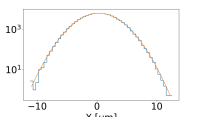
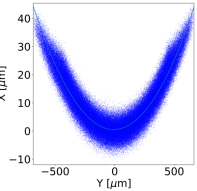
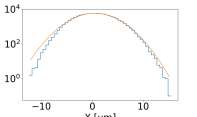
To gain more insight into the problem of spectral resolution degradation in mirror systems with  $\varepsilon$ , Sec. IV B 1, we study the reduced image size dependence on the focal length  $f_2$ . The results are shown in Fig. 13. If the angular aperture of the system is relatively small ( $\Upsilon_v = \Upsilon_h = 1.5$  mrad, solid lines), the reduced size for both of the elastic ( $\varepsilon = 0$ , blue) and inelastic ( $\varepsilon = 4$  meV, green) images change almost linearly with  $f_2$ . In the large- $f_2$  range, the elastic lines (blue) approach the reference case of imaging with ideal lenses (red lines). The inclination is defined by the magnification factor of the refocusing system  $b_{\cup R} f_2 / f_1$ . If the horizontal acceptance is increased to  $\Upsilon_h = 10$  mrad (dashed lines), the result does not change much for the KB mirrors, see Fig. 13(b). However, in the case of the paraboloids, see Fig. 13(a), the linear behavior breaks down and the reduced image size increases dramatically, albeit with one exception. For  $f_2 = 1.471$  m, which corresponds to the 1:1 imaging case, the image sizes are exactly the same as for the small angular aperture case (solid lines). This is probably related to the fact that the Abbe sine condition for two parabolic mirrors is perfectly fulfilled in the 1:1 imaging case [6]. Montel systems perform similarly to KB systems; however, the image size increases quickly with increases in the horizontal angular aperture.

The results of the studies presented in Fig. 13 provide another example of the superior performance of KB systems compared to Montel and paraboloidal mirrors. However, no optimal  $f_2$  value can be found in any of the considered mirror cases, which would eliminate or mitigate the degradation of the spectral resolution with  $\varepsilon$ , if the pixel detector is placed perpendicular to the optical axis.

Figure 14 and 15 show the magnitude of the inelastic waist vs. deviation from reference image plane for paraboloidal and Montel mirror systems. These results of the simulations should be compared with the those calculated for the KB-mirror systems shown in Figs. 6 and 7, respectively.

Figure 16 shows the performance characteristics of the refocusing systems comprising either paraboloidal or Montel mirrors. These should be compared with the performance characteristics of the refocusing systems composed of KB-mirrors in Fig. 8.

TABLE VII: Beam cross sections in image plane 2 calculated for the elastic scattering case  $\varepsilon = 0$  for the refocusing system of the x-ray echo spectrometer in four different mirror-crystal configurations with Montel mirror systems as collimating and focusing elements. Two cases of the angular apertures  $\Upsilon_v \times \Upsilon_h$  are considered. Numerical values are provided for the vertical image size  $\Delta\tilde{X}_2$  in image plane 2, reduced image size  $\Delta\tilde{x}_2$ , and for spectral resolution  $\Delta\tilde{\varepsilon}$ . The configuration graphs show side views of the beam trajectories (optical axes). The numbers in the square brackets correspond to calculations with the horizontal angular aperture increased to  $\Upsilon_h = 10$  mrad. The numbers highlighted in gray correspond to best imaging cases.

Configurations	I	II	III	IV
	 $(-\pi-, \pi-, \pi+, 0+ -)$ $G_D < 0$	 $(-\pi+, \pi+, \pi-, 0- -)$ $G_D > 0$	 $(-\pi-, \pi-, \pi+, 0+ +)$ $G_D < 0$	 $(-\pi+, \pi+, \pi-, 0- +)$ $G_D > 0$
$\Upsilon_v = 1.5$ mrad $\Upsilon_h = 1.5$ mrad	 	 	 	 
$\Upsilon_v = 1.5$ mrad $\Upsilon_h = 10$ mrad	 	 	 	 
$\Delta\tilde{X}_2$ [ $\mu\text{m}$ ]	33.94 $\pm$ 0.08 [42.7 $\pm$ 0.2]	34.16 $\pm$ 0.03 [40.7 $\pm$ 0.1]	33.82 $\pm$ 0.04 [49.1 $\pm$ 0.1]	34.66 $\pm$ 0.08 [43.7 $\pm$ 0.2]
$\Delta\tilde{x}_2$ [ $\mu\text{m}$ ]	5.65 $\pm$ 0.01 [8.56 $\pm$ 0.02]	5.39 $\pm$ 0.01 [6.49 $\pm$ 0.02]	5.38 $\pm$ 0.01 [6.48 $\pm$ 0.02]	5.66 $\pm$ 0.01 [8.40 $\pm$ 0.02]
$\Delta\tilde{\varepsilon}$ [ $\mu\text{eV}$ ]	113.0 $\pm$ 0.2 [171.2 $\pm$ 0.4]	107.9 $\pm$ 0.3 [129.9 $\pm$ 0.3]	107.6 $\pm$ 0.2 [129.7 $\pm$ 0.3]	113.2 $\pm$ 0.3 [168.0 $\pm$ 0.4]



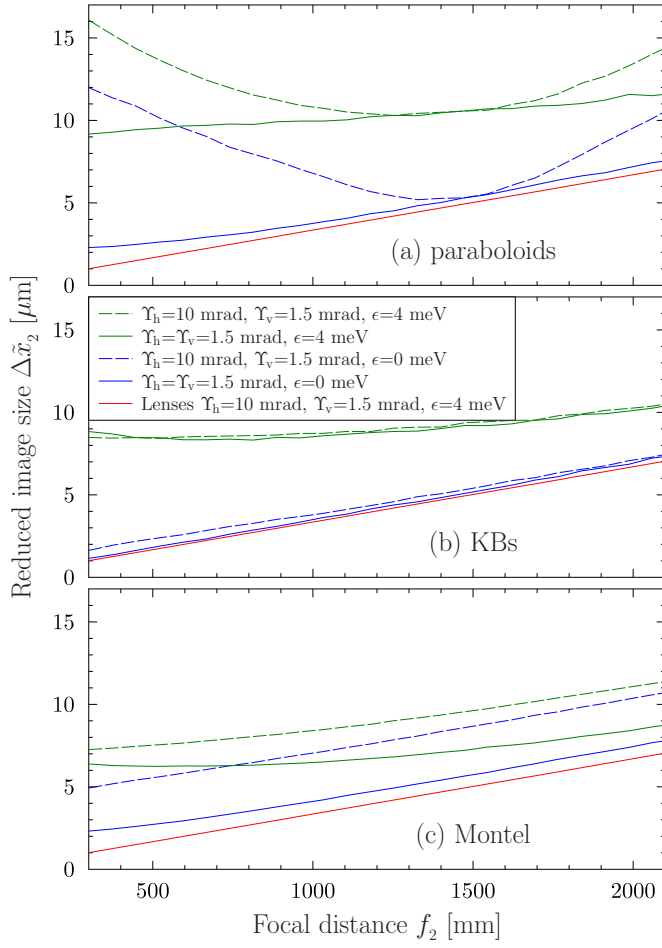


FIG. 13: Reduced image size in image plane 2 versus focal distance  $f_2$  of the imaging optical systems  $F_2$  calculated for the refocusing system with (a) the paraboloidal mirrors, (b) KB-mirror systems, and (c) Montel systems, all in configuration I (see [Tables II-III](#)) for different values of the angular apertures  $\Upsilon_h$  and  $\Upsilon_v$ . Red lines show results of calculations for the ideal lens case, as a reference.

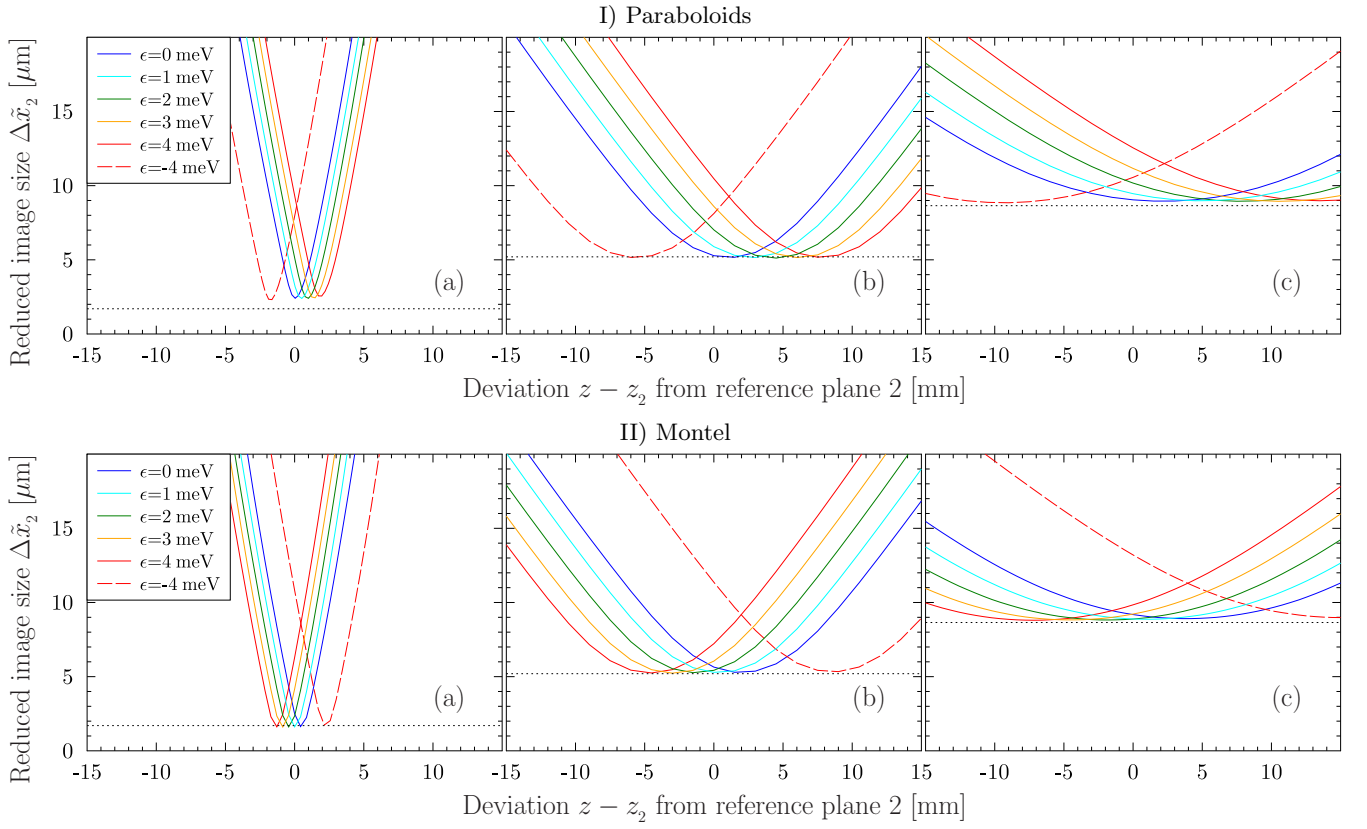


FIG. 14: Reduced vertical image size  $\Delta\tilde{x}_2$  as a function of deviation  $z - z_2$  from reference image plane 2, calculated for different energy transfer values  $\varepsilon$  and for selected focal length values  $f_2$  of imaging mirror  $F_2$ : (a)  $f_2 = 0.4$  m, (b)  $f_2 = 1.471$  m, and (c)  $f_2 = 2.5$  m. Presented here are results for I) paraboloids, and II) Montel mirror systems, with the angular apertures  $\Upsilon_v = \Upsilon_v = 1.5$  mrad. All mirror systems feature very similar results. Mirror arrangement corresponds to configuration I in Tables II, III, and VII.

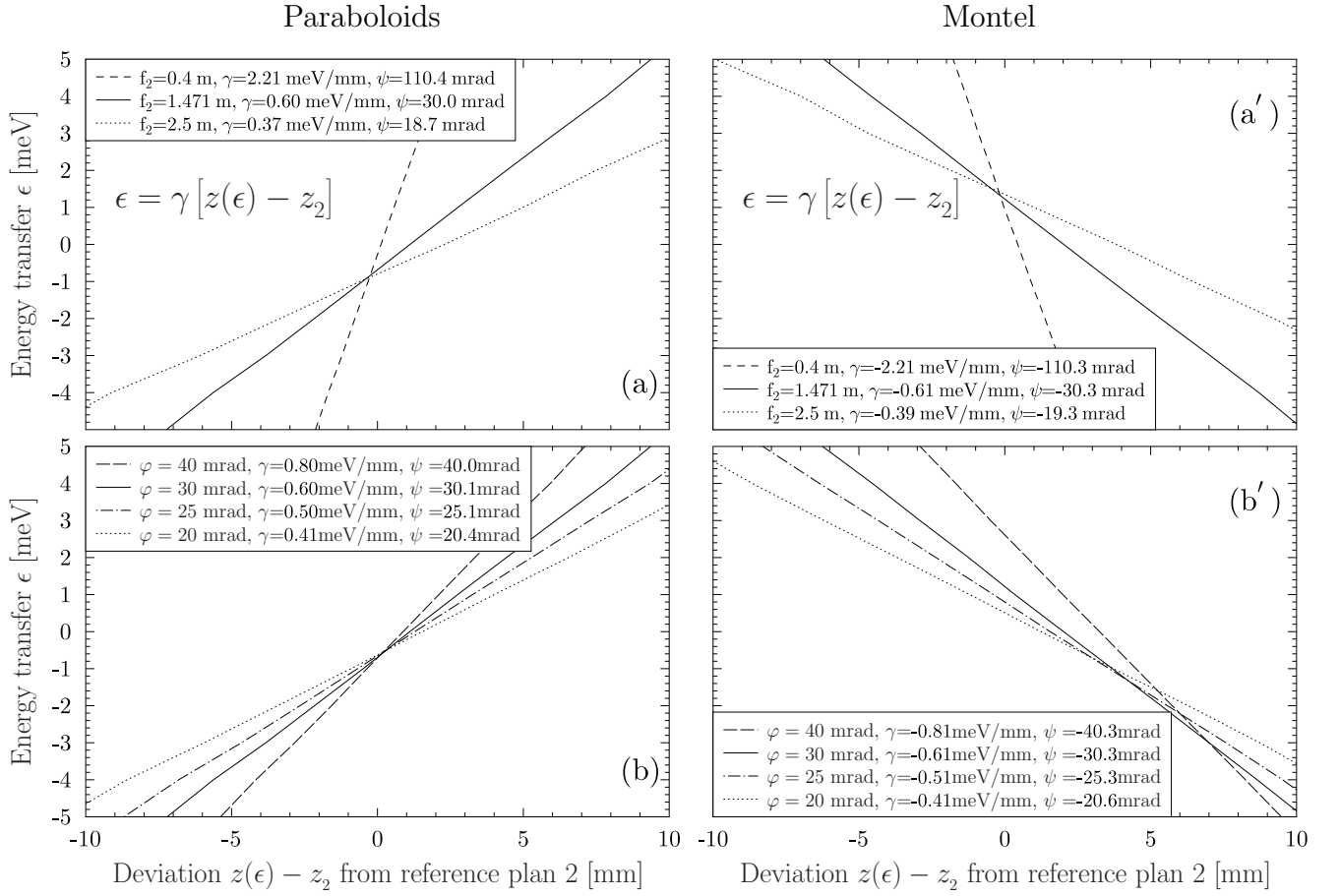


FIG. 15: Correspondence between the energy transfer  $\epsilon$  and the deviation  $z(\epsilon) - z_2$  from reference plane 2 of the reduced image with the smallest size. Calculated for paraboloidal mirrors case (left) and Montel mirrors case (right). To be compared with the data for the KB-mirrors case in Fig. 7(a)-(b). The results are derived from data in Fig. 14 for selected focal length values  $f_2$ . Mirrors' incidence angle is  $\phi = 30$  mrad and angular apertures  $\Upsilon_v = \Upsilon_h = 1.5$  mrad. (b)-(b') Calculated with  $f_2 = 1.471$  m (1:1 imaging) and selected values of glancing angle of incidence  $\phi$ .

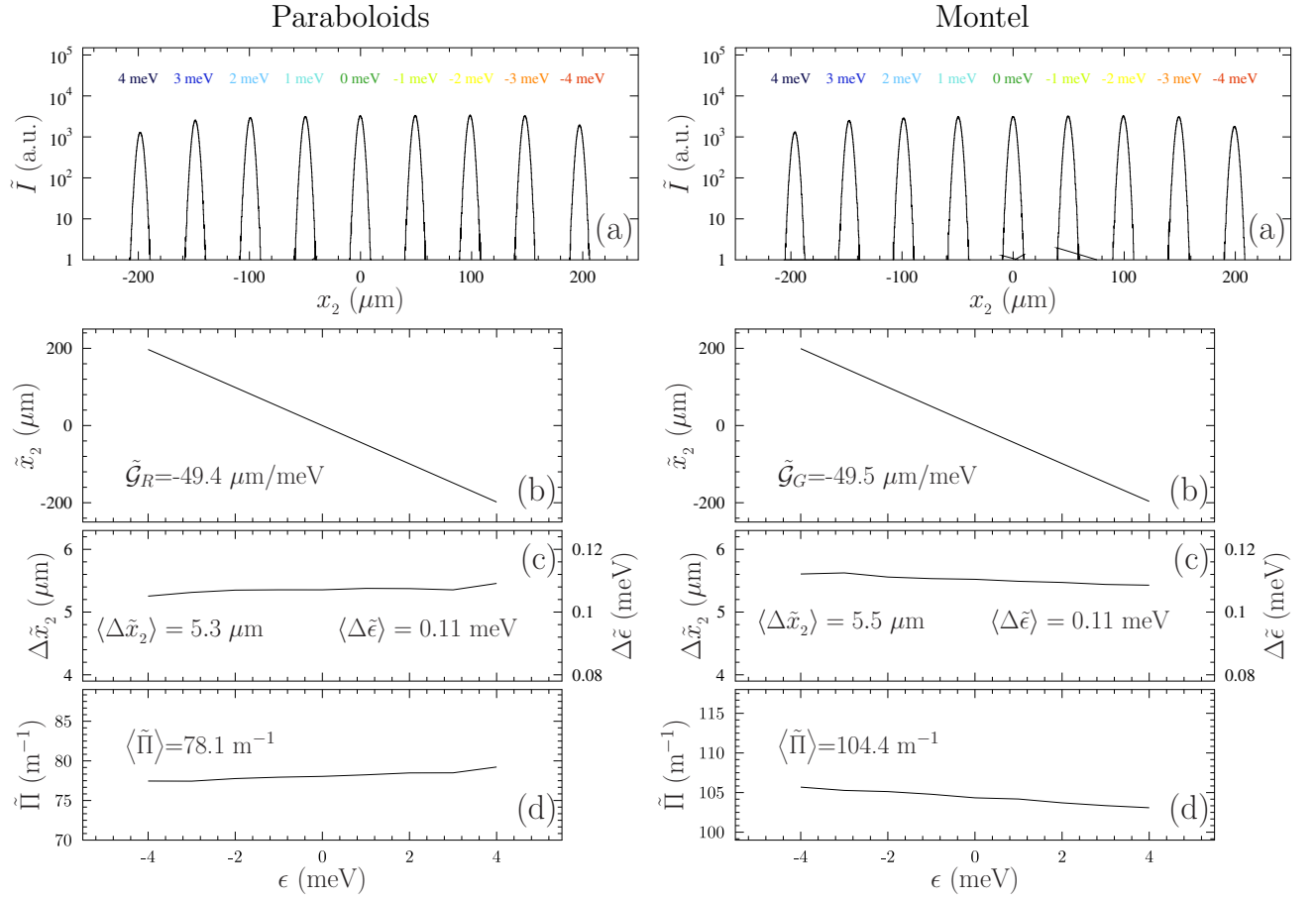


FIG. 16: Performance characteristics of the x-ray echo spectrometer with the refocusing system composed of paraboloidal mirrors (left column) and Montel mirror systems (right column): (a) Reduced image profiles calculated for various values of energy transfer  $\epsilon$  in inelastic x-ray scattering under the same conditions as in Fig. 5, however, with the IXS spectra imaged on the oblique image plane. (b) Image peak position  $\tilde{x}_2$ , (c) reduced image size  $\Delta\tilde{x}_2$ , and (d) curvature  $\tilde{\Pi}$  of the best-fit parabola to the image profile as a function of  $\epsilon$ . Compare with the similar results of Figs. 6 and 11 presented for the case of lenses and KB-mirror systems, respectively.